Cohesive granular materials composed of nonconvex particles

Baptiste Saint-Cyr, Farhang Radjai, Jean-Yves Delenne, Philippe Sornay

Cohesive granular materials composed of nonconvex particles

Baptiste Saint-Cyr,[1,2,*] Farhang Radjai,[1,†] Jean-Yves Delenne,[3] and Philippe Sornay[2]

[1]*LMGC, Université Montpellier 2-CNRS, Place Eugène Bataillon, F-34095 Cedex, France*
[2]*CEA, DEN, SPUA, LCU, F-13108 Saint Paul lez Durance, France*
[3]*IATE, UMR 1208 INRA-CIRAD-Montpellier Supagro-UM2, 2 place Pierre Viala, F-34060 Cedex, France*

The macroscopic cohesion of granular materials made up of sticky particles depends on the particle shapes. We address this issue by performing contact dynamics simulations of 2D packings of nonconvex aggregates. We find that the macroscopic cohesion is strongly dependent on the strain and stress inhomogeneities developing inside the material. The largest cohesion is obtained for nearly homogeneous deformation at the beginning of unconfined axial compression and it evolves linearly with nonconvexity. Interestingly, the aggregates in a sheared packing tend to form more contacts with fewer neighboring aggregates as the degree of nonconvexity increases. We also find that shearing leads either to an isotropic distribution of tensile contacts or to the same privileged direction as that of compressive contacts.

PACS number(s): 45.70.−n, 83.80.Fg, 61.43.Gt

I. INTRODUCTION

Cohesive granular materials are at the heart of a variety of engineering applications in particle processing, soil mechanics, and powder technology. The shear strength of such materials can be split into an internal angle of friction, as in cohesionless materials, and a macroscopic cohesion, which reflects the aptitude of the material to sustain tensile stresses [1,2]. This cohesion in combination with granular disorder has drastic effects on the equilibrium states. The angle of repose increases with cohesion and the material can be molded into arbitrary shapes. The packing fraction may vary in a broader range and often long force chains build up despite locally loose structures [3]. The properties of compressibility and flowability are essential for the manufacture of homogeneous and resistant compacts in powder technology [4]. Cohesive granular materials have been investigated by experiments and numerical simulations for a better understanding of the scale-up of interactions between the particles. Very loose packings characterized by low connectivity and chainlike structures have been evidenced in assemblies of nano-sized particles governed by van der Waals forces [5]. Loose cohesive powders and the dynamics of pore collapse during the compaction process have been extensively studied by the discrete element method (DEM), which provides direct access to the particle-scale information and underlying physical mechanisms [3,6–9]. The compaction of ceramic and metallic powders have been modeled by DEM simulations [10–13]. The shear strength and force distributions of wet granular packings have been studied as a function of water content and the size polydispersity of the particles [14–16]. DEM simulations have also been used to investigate the flow properties of cohesive granular materials [17–22].

However, all reported studies of cohesive granular materials by discrete element modeling have dealt with spherical particles. Most granular materials have complex particle shapes characterized by various degrees of angularity (e.g.,

geomaterials), elongation, platiness (e.g., biomaterials), and nonconvexity (e.g., sintered powders). Ceramic powders are most of time composed of aggregates or clusters of elementary particles (cristallites) [23]. In the case of UO_2 powders, these aggregates have complex dendritic shapes. The nonconvexity of the aggregates varies from superficial roughness of their surface to deep concavity allowing for interlocked structures that control the geometrical and mechanical properties of the material.

Particle shape effects have been investigated in cohesionless granular materials by considering quasistatic rheology (shear strength, dilatancy), packing properties (texture, pore size distribution), and force transmission. A rather counterintuitive finding is that the packing fraction, first, increases before declining again when the particles increasingly deviate from spherical shape [24–29]. The internal friction angle is found to increase with the angularity and elongation of soil particles [30–37]. By a detailed comparison between packings of polygonal particles and circular particles endowed with rolling friction, it was recently shown that, by hindering particle rotations, a rolling friction coefficient may mimic particle shape effects with respect both to shear strength and packing fraction [38]. This hindering or interlocking effect has also been evidenced for aggregates of spherical particles [39–45]. Granular materials develop an anisotropic contact network under shearing, and DEM simulations indicate also that enhanced structural anisotropy due to shape anisometry underlies the increase in shear strength [27,46].

The issue that we would like to address in this paper is how the macroscopic cohesion is influenced by particle shape. We consider a 2D model of nonconvex particles in which the degree of nonconvexity can be varied and that can easily be simulated by DEM. The model particles are rigid aggregates of three overlapping disks with a threefold rotational symmetry. Their nonconvexity can be tuned by adjusting the overlap, the range of shapes varying thus from simple disk when the three disks components fully overlap, to a trimer built by three tangential disks. This model shape was previously used to analyze the strength and packing properties of cohesionless packings [28]. The contact dynamics method is employed for the simulations and the adhesion force is assumed to occur at

---

*baptiste.saint-cyr@univ-montp2.fr
†franck.radjai@univ-montp2.fr

the contact points between aggregates as a tensile threshold on the normal force. Due to multiple contacts between two particles, the cohesion increases with nonconvexity. But, as we shall see, the shape dependence is rather complex and characterized by fluctuations of the macroscopic cohesion as a function of nonconvexity. Only the macroscopic cohesion resulting from the unconfined yield stress of the packing is monotonic as a function of nonconvexity. The high variability of packing fraction leads to strong stress or strain concentration that does not allow for a homogeneous expression of cohesion within the packings. We consider different configurations and the spatial variabilities as well as the mean values. We show that the nonconvexity contributes to create more porous structures but better connected.

We first introduce in Sec. II the technical details of our simulations, the nonconvexity parameter, the procedure of sample preparation and relevant mechanical observables, which are essential for the interpretation of the results. In Sec. III, we study the evolution of the mechanical strength as a function of nonconvexity. Secs. IV and V are devoted to the analysis of the granular structure. We conclude with a discussion of the most salient results of this work.

II. NUMERICAL METHOD AND SYSTEM PARAMETERS

A. Particle shape parameter

The particles are regular aggregates of three overlapping disks of the same radius r, as shown in Fig. 1. The particles are assumed to be uncrushable and treated as a single rigid particle. Their shape can be characterized by considering the radius R of the circumscribing circle as compared to the radius R' of the inscribed circle. The difference $\Delta R = R - R'$ represents the concavity of the aggregate, i.e., the inward deviation from the surface of the circumscribing circle. Hence, we define the nonconvexity η of an aggregate by the ratio

$$\eta = \frac{\Delta R}{R}. \qquad (1)$$

It varies from $\eta = 0$, corresponding to a disk, to $\eta \simeq 0.73$, corresponding to a *trimer* of three disks of vanishing overlap.

The parameter η is related to the "roundness" parameter expressed in geology as the ratio of the average radius of curvature of the edges or corners to that of the maximum inscribed sphere [47,48]. With our notations, the roundness of the aggregates is simply $r/[(1 - \eta)R]$, which decreases from 1.72 to $\simeq 0.367$ as η varies from zero to 0.73.
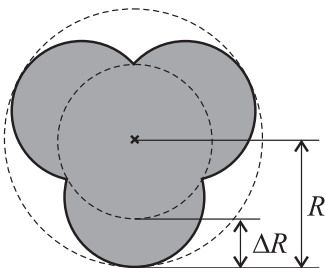

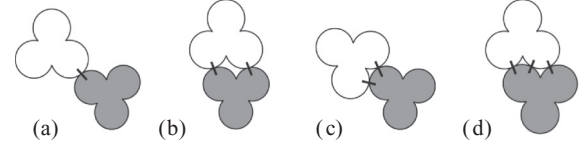FIG. 1. Geometry of a model aggregate used in numerical simulations.

FIG. 2. Four different contact types between two aggregates: (a) simple, (b) double simple, (c) double, and (d) triple.

The nonconvex shape allows the aggregates to touch one another at one, two, or three contact points as shown in Fig. 2. We distinguish four contact types: (1) simple contact (S), (2) double-simple (DS) contact, defined as two simple contacts between two pairs of disks belonging to the aggregates, (3) double (D) contact, defined as two contacts between one disk of one aggregate with two disks of the other aggregate, and (4) triple (T) contact, defined as the combination of one simple and one double contact. While the physical effects related to multiple contacts are essential, as we shall see in Sec. II, their numerical treatment is similar to contacts between disks since each individual contact point is a contact between two disks belonging to two different aggregates.

B. Numerical method

The aggregates are assumed to be perfectly rigid so the relevant kinematic variables attributed to each potential contact are the relative normal velocity u_n and the sliding velocity u_t. The variable u_n is the separation velocity defined as the time derivative of the gap δ_n between two disks, with a positive sign when two disks get separated. The conjugate force variables are the normal force f_n and friction force f_t, respectively.

The frictional-cohesive laws governing sticky contacts consist of piecewise linear graphs relating u_n and f_n, on one hand, and u_t and f_t on the other hand, as shown in Fig. 3. The first graph, called also Signorini's graph [49,50], represents the set of admissible values of u_n and f_n at a contact point ($\delta_n = 0$) between two disks. The positive definiteness of u_n reflects the unilateral nature of contact (no interpenetration). The normal force f_n may take arbitrarily large positive values, but it is bounded by a lower threshold $-f_{nc}$, which defines the adhesion force between two disks. Depending on the physicochemical nature of adhesion, the force $f_{nc} \geqslant 0$ may depend on the particle size as in the case of capillary bonds [51,52]. For the sake of simplicity, and since we focus on the effect of particle shape, we assume here a constant value of f_{nc}. The dependence of f_{nc} is important only for highly polydisperse systems.
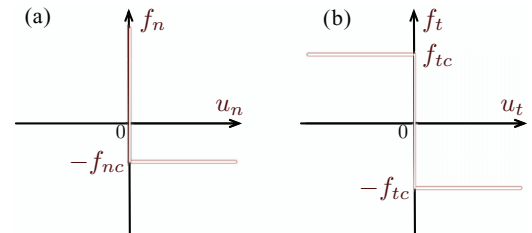

FIG. 3. (Color online) Graphs of a frictional-cohesive contact law: (a) Signorini's graph for normal forces and (b) Coulomb's graph for friction forces. The friction force threshold is given by equation (2).

An essential feature of Signorini's graph is that it cannot be reduced to a (single-valued) function (f_n as a function of u_n or the reverse). It is a "complementarity relation" in the sense that at least one of the two variables is zero [53]. In a purely numerical treatment, however, this relation may be regularized by replacing the vertical branch of the graph by a linear dependence of finite slope representing a fictitious viscosity. In the molecular dynamic method, for example, the normal force is expressed as a function of δ_n with a slope expressing the contact stiffness. But the implicit time-stepping scheme of the *contact dynamics* (CD) method, used in this work, allows for an exact treatment of Signorini's graph [49,50,54–56].

The second graph in Fig. 3 is the Coulomb friction law represented by the set of the admissible values of u_t and f_t at a contact point. The friction force threshold f_{tc} for a noncohesive contact is μf_n, where μ is the friction coefficient. But this threshold for a sticky contact is enhanced due to the effect of the adhesion force f_{nc}. In the simplest approximation, we have

$$f_{tc} = \mu(f_n + f_{nc}). \tag{2}$$

This friction threshold vanishes only when $f_n = -f_{nc}$, i.e., at incipient separation between two particles. It should also be remarked that, in the same vein as Signorini's condition, Coulomb's graph is a complementarity relation. It can be regularized by replacing the vertical branch by a linear relation and a fictitious tangential viscosity but is implemented without regularization in the framework of the CD method described in more detail in the Appendix.

C. Sample preparation

The samples are prepared by the same procedures as those reported in Ref. [28]. Each sample is composed of 5000 aggregates for eight different values of $\eta \in [0, 0.7]$. To avoid long-range ordering, a size polydispersity was introduced by taking R in the range $[R_{\min}, R_{\max}]$ with $R_{\max} = 3R_{\min}$ and a uniform distribution of particle volumes ($\propto R^{-2}$), which leads to a high packing fraction ρ [57–60]. It is worth mentioning that a lower level of size polydispersity might be sufficient for topological disorder (disorder in the connectivity of the particles and force transmission) but does not lead to appreciable metric disorder of the contact network.

A dense packing composed of disks ($\eta = 0$) was first constructed by means of random pluviation of the aggregates into a rectangular box of dimensions $l \times h$. For other values of η, the same packing was used with each disk serving as the circumscribing circle. The aggregate was inscribed with the given value of η and random orientation inside the circle. This geometrical step was followed by isotropic compaction of the packings by the contact dynamics method inside a rectangular frame. The gravity g and friction coefficients μ and μ_w between the aggregates and with the walls, respectively, were set to zero during compaction in order to optimize the packing homogeneity. The samples prepared by this procedure are isotropic, isostatic, and dense. Two snapshots of the initial packing configurations for $\eta = 0$ and $\eta = 0.7$ are shown in Fig. 4.

The isotropic samples for all values of η were subjected to two different tests:

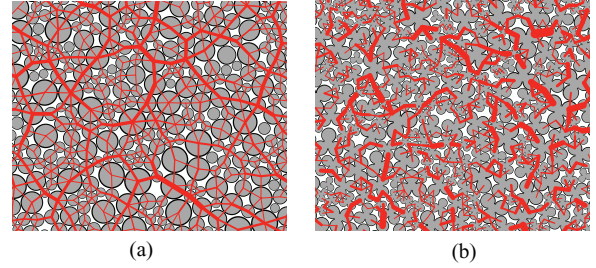(a)   (b)

FIG. 4. (Color online) Snapshots of the initial packing configuration for $\eta = 0$ (a) and $\eta = 0.7$ (b). The line thickness is proportional to the normal force acting at the contact points between aggregates.

(i) Biaxial compression: The granular sample is sheared by applying a slow downward velocity $\dot{\varepsilon}_{yy}$ on the top wall with a constant confining stress acting on the lateral walls. The friction coefficient is set to 0.5 between aggregates and to 0 with the walls. The zero friction with the walls prevents from stress gradients as those that lead to the Janssen effect [61].

(ii) Simple compression: The two side walls are removed and a vertical stress σ_{yy}^0 is applied on the top wall. We keep the same friction coefficient $\mu = 0.5$ between the aggregates as in the biaxial compression tests but the friction coefficient μ_w between the aggregates and the top and bottom walls is set to 1 to prevent sideways slip of the sample. The sample may slip sideways as a result of slightest asymmetry about the vertical axis without friction. But with friction, it reaches a state of static equilibrium under the action of the initial stress σ_{yy}^0 due to adhesion forces between aggregates. The sample is then compressed by increasing incrementally the vertical stress σ_{yy}.

These tests will be described in more detail in the following sections. They are meant to measure the macroscopic strength of the packings in terms of the internal angle of friction and Coulomb cohesion as a function of shape parameter η and adhesion of the aggregates. Animation videos of the simulations are available at www.cgp-gateway.org/ref015.

D. Dimensionless parameters

The state of the packing can be characterized by two dimensionless numbers: bond number B and inertia number I. For undeformable aggregates, the adhesion force f_{nc} is the only internal force and it should be compared to the repulsive contact forces induced by the confining stress. Hence, the "effective" cohesion of the system is characterized by a *bond number* defined as

$$B = \frac{f_{nc}}{pd}, \tag{3}$$

where p is the average stress and d is the mean aggregate diameter [3,6,9,52,62,63]. A granular material with weak adhesion force can have a large bond number at low confining pressure. This is the case of wet fine sand, for example, which can easily be shaped into sand arts on a beach [15].

The inertial number I represents the inertial particle displacements as compared to the driving strain. For a vertical shear rate $\dot{y}/y$, we have (in 2D) [64]

$$I = \frac{\dot{y}}{y}\sqrt{\frac{m}{p}}, \tag{4}$$

where m is the average mass of an aggregate and p is the mean 2D pressure. In our simulations, I was kept below 10^{-3} in different tests, corresponding to quasistatic conditions.

III. MACROSCOPIC COHESION

The mechanical strength of the packings is evaluated by the Mohr-Coulomb criterion which is represented by the following failure envelope in 2D:

$$q = p \sin \varphi + c \cos \varphi, \qquad (5)$$

expressing the stress deviator $q = (\sigma_1 - \sigma_2)/2$ as a linear function of the average stress $p = (\sigma_1 + \sigma_2)/2$, where σ_1 and σ_2 are the principal stresses. The internal angle of friction φ and Coulomb cohesion c are material parameters at well-defined states of the material such as the shear stress peak state and the residual state reached after a long shearing. We consider below different tests performed to extract the values of φ and c.

A. Biaxial compression

To estimate the values of c and φ, we use biaxial compression tests with three different values of p for each value of nonconvexity η. The three tests are performed starting with the same initial isostatic states briefly described in the Sec. II. The same downward velocity $\dot{\varepsilon}_{yy}$ is used for all the tests and for all packings. The adhesion parameter f_{nc} is the same although the bond number B defined by (3) varies with p. Figure 5 shows the normalized shear stress q/p as a function of the cumulative shear strain ε_q for different values of η and $p = 7.5$ MPa, $B = 2.66$, and $I \simeq 10^{-4}$. The shear stress q/p increases rapidly to a peak value before softening and reaching a residual or "critical" value. The initial peak reflects the high initial packing fraction and the rigidity of the aggregates. The critical state strength and packing fraction are independent of the initial state and depend only on η. For a given value of the initial packing fraction, the peak stress also represents an objective measure of the strength depending only on the parameter η. Both the peak and critical-state values of q/p increase with η.

Figure 6 presents the (p,q) values at the peak state for three values of the mean stress p and different values of η. Figure 7 shows the pairs of points (p,q) averaged this time in the residual state with error bars representing the standard
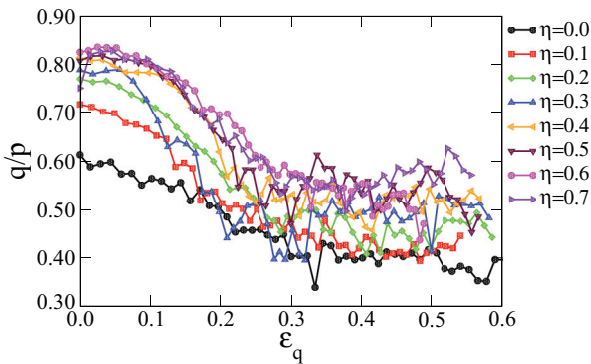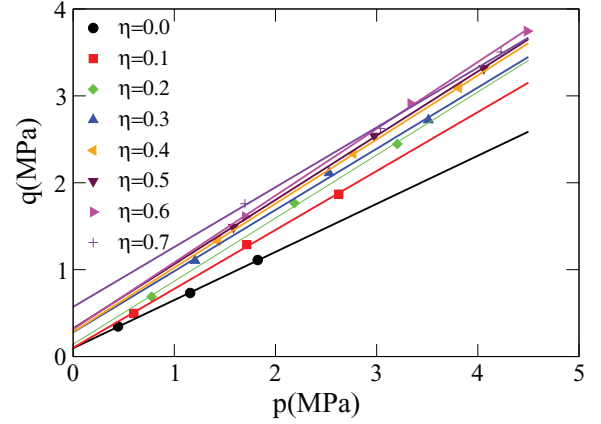

FIG. 6. (Color online) The peak strength envelopes for different values of the shape parameter η.

deviation of the fluctuations. As expected, the data are well fitted by affine Mohr-Coulomb failure envelopes, with a linear correlation coefficient of $\simeq 0.99$.

We extract from the Mohr-Coulomb envelops the internal angles of friction φ^{peak} and φ^* given by the slope for the peak state and residual state, respectively, as well as the corresponding cohesion parameters c^{peak} and c^*, as a function of η. These data are displayed in Figs. 8, 9, 10, and 11.

The internal friction angle at the peak and residual states increase as a function of η for the packings of cohesive aggregates. Figure 8, shows that φ steadily increases with η in these two states and tend to saturate as it was observed previously in the cohesionless case [28] and as we see for φ^* in Fig. 9. As expected, φ^* is not affected by adhesion between particles. We also note that for $\eta \geqslant 0.1$ the difference between φ^{peak} and φ^* is nearly constant and is larger than that of the disk packing ($\eta = 0.0$). The saturation of the values of the internal friction angle at large nonconvexity was analyzed in Ref. [28] and shown to reflect the interlocking of the aggregates.

The peak cohesion c^{peak} increases steadily as η varies from 0 to 0.7. But discontinuous changes are observed in the ranges [0.2,0.3] and [0.6,0.7]. c^{peak} is nearly multiplied by a factor 8 between $\eta = 0$ and $\eta = 0.7$. This increase of cohesion for a constant value of the local tensile threshold f_{nc} between the aggregates clearly demonstrates that the

FIG. 5. (Color online) Normalized shear stress q/p as a function of the cumulative shear strain ε_q for different values of the shape parameter η.
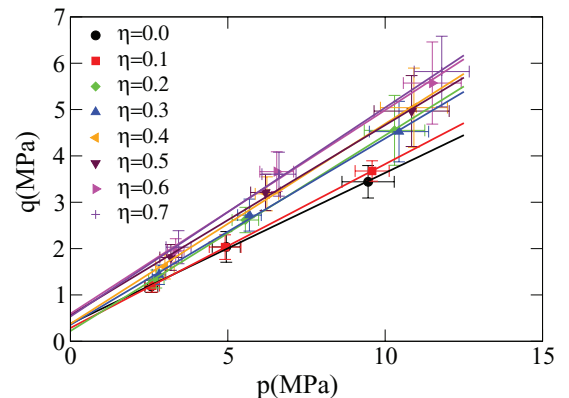

FIG. 7. (Color online) The residual strength envelopes for different values of the shape parameter η.
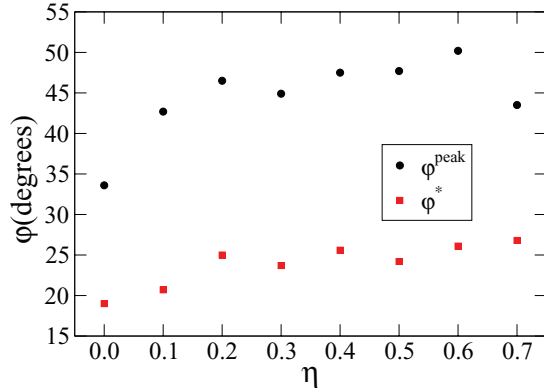
FIG. 8. (Color online) Internal friction angle φ at the peak state and in the sheared state as a function of η.

FIG. 10. The macroscopic cohesion c^{peak} at the peak state as a function of η.

effect of local adhesion is amplified by nonconvex particle shape to enhance the macroscopic cohesion. Surprisingly, the residual-state cohesion c^* does not offer a similar trend and fluctuates instead as η is increased. c^* declines between $\eta = 0$ and $\eta = 0.2$ and then increases between $\eta = 0.2$ and $\eta = 0.6$ and, finally, slightly declines at $\eta = 0.7$. Moreover, the values of c^* are by one order of magnitude below those of c^{peak}. This discrepancy and discontinuous changes indicate that the cohesion is only partially expressed. A snapshot of the packing in the residual state is shown in Fig. 12 for $\eta = 0.3$ where we observe very pronounced shear bands characterized by high porosity and spanning the whole packing. We also observe that the patterns of shear bands vary with the evolution of the system due to the motions of the walls and strongly fluctuate for different values of η.

These features, partially related to the boundary conditions, indicate that, in contrast to the internal friction angle, the macroscopic cohesion is sensitive to such inhomogeneities. The cohesion of the material can fully manifest itself only if the tensile forces are uniformly mobilized throughout the system. This is clearly not the case as c^* is not a well-defined function of η and c^{peak} shows irregular changes. But the larger values of c^{peak} are consistent with a more uniform deformation at the peak state, where the shear bands begin to develop, as
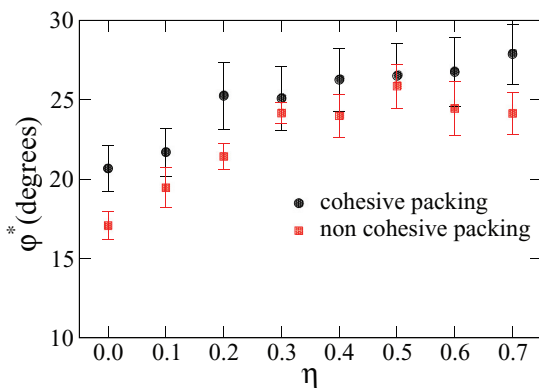
compared to the residual state, where the extent of shear bands and their porosity are further developed.

The issue raised by this irregular behavior of the macroscopic cohesion is whether we can get larger values of cohesion by loading the same packings differently. In particular, the largest cohesion is expected for the largest connectivity, which is the case of the initial state prepared by isotropic compaction, and for the most diffuse deformation allowing the adhesion forces between the aggregates to be mobilized. Since the walls seem to enhance shear bands, we analyze in the next section the same samples subjected to unconfined compression.

B. Unconfined yield strength

In unconfined tests, known also as simple compression test, the lateral stress σ_{xx} is set to zero and the sample is deformed along the y direction. Assuming that the principal stress directions σ_1 and σ_2 are the same as those of the sample, we have $\sigma_1 = \sigma_{yy}$ and $\sigma_2 = 0$. As a consequence, the stress ratio is $q/p = 1$ and, thus, the Coulomb criterion implies that the unconfined cohesion is given by

$$c^u = \frac{1}{2}\sigma_{yy}^{\text{rupt}}\frac{1 - \sin\varphi}{\cos\varphi},\tag{6}$$

where $\sigma_{yy}^{\text{rupt}}$ is the yield stress in simple compression and φ is the peak value of the internal friction angle evaluated at the peak state by biaxial shearing, as shown in Fig. 8.

FIG. 9. (Color online) Internal friction angle φ in the sheared state as a function of η for both the cohesive and noncohesive packings. Error bars represent the standard deviation.

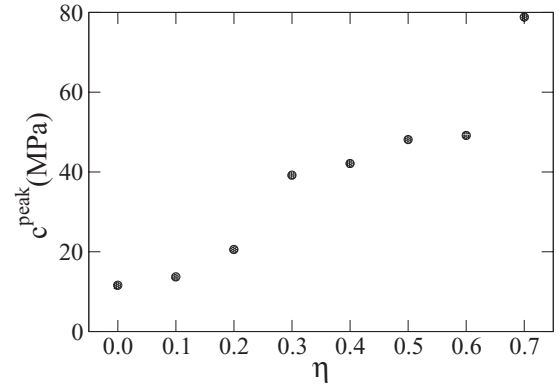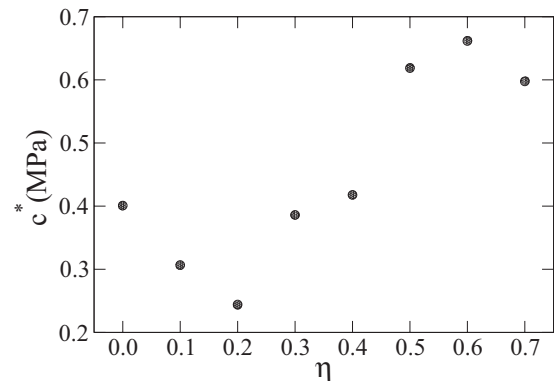FIG. 11. The macroscopic cohesion c^* in the residual state as a function of η.
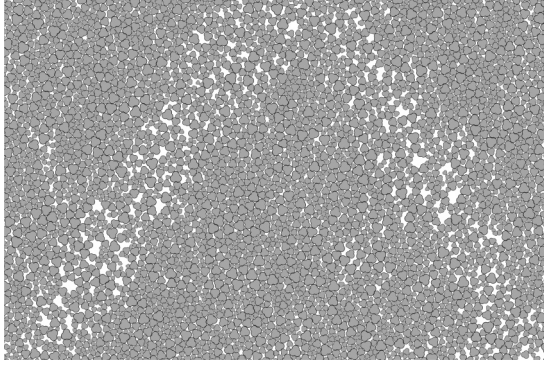
FIG. 12. A snapshot of a cohesive sample for $\eta = 0.3$ in the residual state where we observe shear bands, which can be distinguished by their higher porosity.

We start with the samples prepared by isotropic compression under a stress of $\sigma_{yy}^0 = 10$ MPa without friction between the aggregates. The side walls then are removed and a load of 10 MPa is applied on the upper wall. The samples keep their mechanical equilibrium without deforming. At this point, we have $B \simeq 1.89$ for all samples. In order to prevent the samples from sidewise slip, we also set the friction coefficient μ_w between the aggregates and the top and bottom walls to 1. All other parameters have the same values in biaxial compression tests.

Figure 13 shows the normalized vertical stress as a function of the vertical strain ε_{yy} for different values of η. As in biaxial compression (see Fig. 5), the vertical stress increases rapidly to a peak value and then declines much faster than in biaxial compression tests. This difference is clearly related to the fact that the material under unconfined conditions is unstable and tends to fail by strain localization as discussed below. The fact that σ_{yy} does not fall off to zero after the peak stress is due to the reversible nature of the adhesion law. Figure 14 shows the cohesion c^u calculated from Eq. (6) as a function of η. c^u declines nearly linearly from $\eta = 0$ to $\eta = 0.6$. The point for $\eta = 0.7$ deviates from this trend and needs to be checked by further simulations. It is remarkable that the cohesion values are almost 10 times higher than those obtained for the peak state in biaxial shear tests; see Fig. 10.

These high values of cohesion suggest that the samples are far more homogeneous at the beginning of unconfined
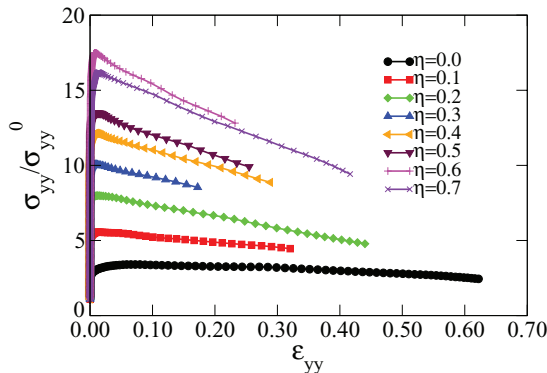

FIG. 13. (Color online) Normalized vertical stress $\sigma_{yy}/\sigma_{yy}^0$ as a function of vertical strain ε_{yy} in unconfined compression tests.
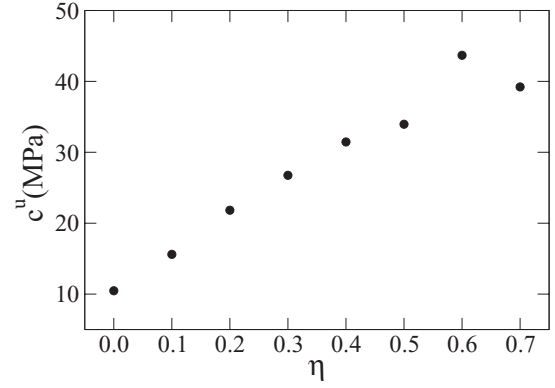

FIG. 14. Macroscopic cohesion as a function of η obtained by unconfined compression tests.

compression. This is what we observe in Fig. 15(a) displaying the force chains for $\eta = 0.5$ at the beginning of unconfined compression. The tensile and compressive forces are statistically homogeneous, with tensile contacts oriented preferentially in the horizontal direction and compressive forces in the vertical direction. We also observe no sign of shear bands at this stage of deformation.

When σ_{yy} approaches its maximum value, a horizontal stress gradient appears inside the packing and the strongest force chains concentrate at the center of the sample, as shown in Fig. 15(b). The stress gradients are a consequence of friction forces with the top and bottom walls mobilized towards the center to resist the motions of the particles towards the left and right free edges of the packing. This effect is similar to the Janssen effect in a silo geometry with an exponential increase of the mean and shear stresses from the left and right edges, where the stress components are zero, towards the center of the sample [65].

Finally, as shown in Fig. 15(c), the sample fails by strain localization. The failure starts out by tensile breakage (mode I) at the center of the sample but continues in mode II along shear bands that divide the sample into four triangular parts. The two vertical triangles are squeezed gradually against each other by vertical shortening of the sample while the two lateral triangles fall apart into small clusters.

From these biaxial and simple compression simulations, we conclude that the macroscopic cohesion of granular materials is strongly dependent on the boundary conditions. The largest measured cohesion represents an intrinsic property of the material and it can be obtained only by homogeneous deformation with a homogeneous mobilization of the adhesion forces along the direction of extension. These conditions are satisfied at the beginning of unconfined compression tests.

IV. PACKING FRACTION

Since the original samples are prepared in a dense state by setting the friction coefficient to zero, they all dilate by shear. But, as a result of inhomogeneous shearing, all parts of the samples do not dilate at the same time. The evolution of the shear bands during deformation leads to a gradual decrease of the packing fraction as the shear bands go through different

FIG. 16. (Color online) Packing fraction as a function of cumulative shear strain during biaxial compression for the different values of η.

The initially high rate of dilation reflects the homogeneous character of deformation at this stage. Dilation continues afterwards only inside shear bands.

The packing fraction ρ is computed by considering the ratio of the total volume of aggregates and the volume of the simulation cell. The volume of one aggregate is given by

$$\mathcal{A} = 3\pi r^2 - 6r^2(\arccos(d^*) - d^*\sqrt{1 - d^{*2}}) + 1.5\alpha r^2$$
$$+ 0.75\sqrt{3}r^2(\sqrt{1 - d^{*2}} - d^*/\sqrt{3})[1 - \cos(\alpha)], \quad (7)$$

where

$$\alpha = 2\arcsin(0.5\sqrt{3 - 3d^{*2}} - d^*/\sqrt{3}) \quad (8)$$

and d^* is the gap between two disks that compose an aggregate and defined by the ratio $d/2r$, where d and r are, respectively, the distance between the two centers and the radius of the disks. The above expression is valid if $0 \leqslant d^* < \sqrt{3}/2$, i.e., when the three disks are fully overlap.

Note that the initial value ρ^{iso} of the packing fraction corresponds to the isostatic packings prepared by isotropic compression. ρ^{iso} does not vary steadily with η, as shown in Fig. 17: It increases with η and then declines beyond $\eta = 0.2$. The larger values of ρ^{iso} for $\eta = 0.1$ and $\eta = 0.2$ as compared to the disk packing ($\eta = 0$) indicates that small values of nonconvexity enhance interlocking between the aggregates [28]. This unmonotonic evolution of the packing fraction with different shape parameters was recently discussed by several
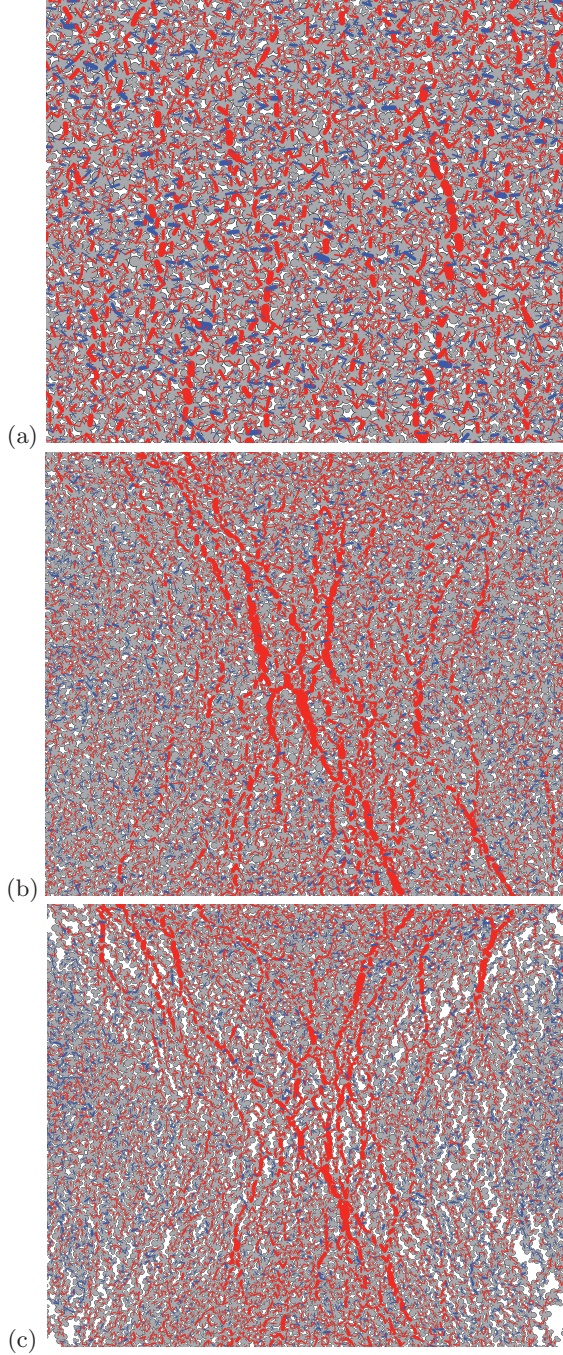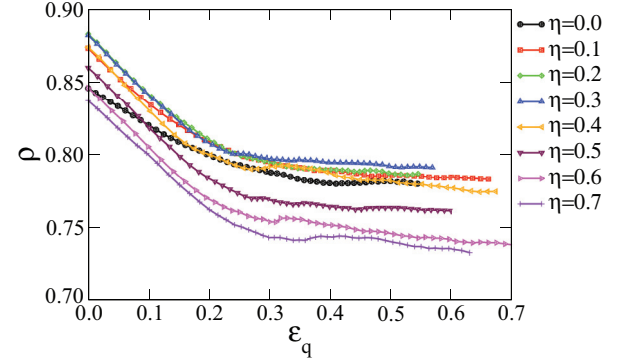

FIG. 15. (Color online) Snapshots of the dense cohesive sample of nonconvex aggregates for $\eta = 0.5$ at the beginning of unconfined compression test (a), at the stress peak (b) and later (c). Line thickness is proportional to the normal force. Compressive and tensile forces are shown in red and blue, respectively.

parts of the sample. In this section, we analyze the evolution of both global and local packing fractions.

Figure 16 displays the packing fraction ρ as a function of the cumulative shear strain ε_q for different values of η in biaxial compression tests. For $\simeq 20\%$ of cumulative deformation, ρ declines at nearly the same rate for all values of η in exception to the disk packing, which dilate at a lower rate. Beyond 20% of deformation, ρ continues to decrease at a much lower rate.
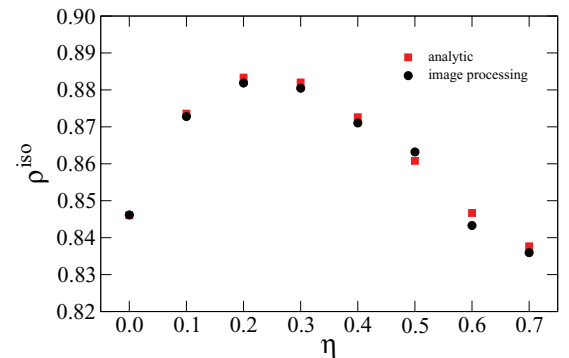

FIG. 17. (Color online) Packing fraction as a function of η in the isotropic state issued from analytic formula (in black) and by image processing (in red).
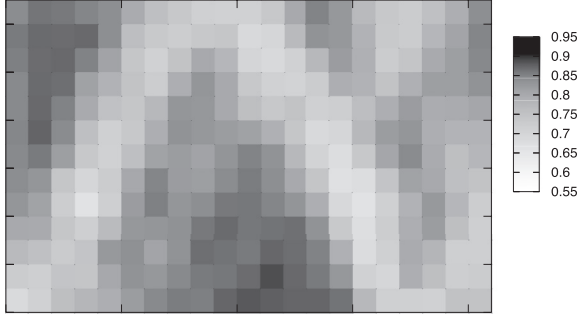
FIG. 18. Map of local packing fractions for the sample $\eta = 0.4$ in the final stage of biaxial compression. The cell size is three times aggregates mean diameter.

authors [24–29,45]. The results of Ludewig *et al.* [45] provide a counterexample indicating that the packing fraction may be monotonic depending on the shape parameter.

In the case of cohesionless rigid aggregates, the "critical" packing fraction ρ^* in the residual state is assumed to be independent of the initial state and, thus, a property of the material. However, as pointed out by many authors, ρ^* is only a "theoretical" packing fraction which should be measured inside the shear bands [66–69]. In the case of cohesive materials, the inhomogeneities are considerably amplified. Hence, the global packing fraction reached after 50% of deformation is still quite far from the low values inside the shear bands corresponding to the true value of ρ^*.

Obviously, the packing fraction at the mesoscopic scales is a crucial parameter in the manufacture of products from cohesive powders. The inhomogeneities in packing fraction (and connectivity) lead to failure problems such as splitting or delamination during discharge and ejection phases of green compacts and influence the quality of the local densification of the greens during sintering. In the following, we briefly investigate the packing fraction distribution at different mesoscopic scales by a pixel-based routine.

For this purpose, the images of the packings are pixelized with solid and void phases represented respectively by black and white pixels. A regular grid of mesh size ℓ_c in multiples of the mean aggregate diameter then is superimposed on the pixelized image. The packing fraction in each mesh is

FIG. 19. (Color online) Evolution of the range of the local packing fraction $\Delta\rho$ as a function of the size of the mesh for the value $\eta = 0$, $\eta = 0.4$, and $\eta = 0.7$ in the isotropic state.
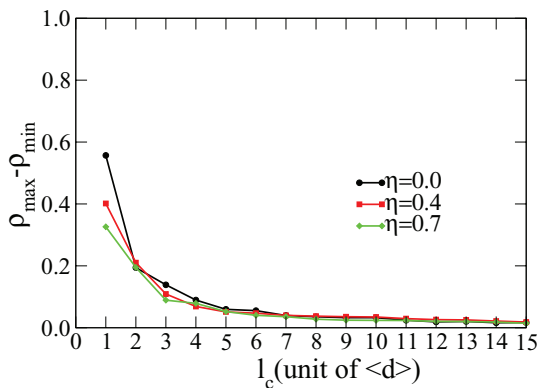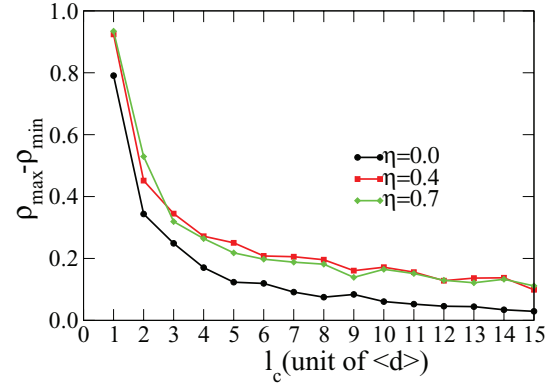

FIG. 20. (Color online) Evolution of the range of the local packing fraction $\Delta\rho$ as a function of the size of the mesh for the value $\eta = 0$, $\eta = 0.4$, and $\eta = 0.7$, in the residual state.

given by the proportion of the pixels representing the solid phase. This method has the advantage of being applicable to granular materials composed of particles of different shapes or issued from experimental observations. An example is shown in Fig. 18, representing a map of local packing fractions in the sample $\eta = 0.4$ in the final stage of biaxial shearing with $\ell_c = 3\langle d \rangle$, where $\langle d \rangle$ represents the mean diameter of the aggregates. While the mean packing fraction is $\simeq 0.8$, the local packing fraction at the considered scale ranges from 0.56 in the shear bands to 0.95 in the most compact parts of the sample.

The packing fraction inhomogeneity can be characterized by the difference $\Delta\rho = \rho_{max} - \rho_{min}$ between the largest value ρ_{max} and the lowest value ρ_{min} of the packing fraction as a function of the scale ℓ_c (cell size in particle diameters). Figures 19 and 20 display $\Delta\rho$ for the packings $\eta = 0.0$, $\eta = 0.4$, and $\eta = 0.7$ in the isostatic packings and in the packings at 40% of cumulative shear strain, respectively. In the isostatic case, $\Delta\rho$ strongly decreases as the cell size varies from ℓ_c to $5\ell_c$ in the three packings. But for larger cell size, $\Delta\rho$ is small ($\leqslant 2\%$) and declines very slowly until $15\ell_c$. The observed small-scale variability reflects the natural porosity of the samples and, hence, it does not depend on the mesh size. The length $\ell_c = 5\langle d \rangle$ may be considered as the size of the representative volume element for the packing fraction in the isotropic state.

In the sheared case, Fig. 20, $\Delta\rho$ decreases from $\ell_c = 1$ to $\ell_c = 7$ and remains practically constant in the range $\ell_c = 7$ to $\ell_c = 15$. The largest value of $\Delta\rho$ is 0.04 for the packing $\eta = 0$ and 0.1 for the packings $\eta = 0.4$ and $\eta = 0.7$. These values roughly correspond to the difference of packing fraction between the shear bands and other parts of the samples. The difference is strongly influenced by shape nonconvexity in transition from $\eta = 0.4$ and $\eta = 0.7$. Clearly, still longer shearing is necessary for the dilation of all parts of the samples.

V. GRANULAR TEXTURE

Beyond packing fraction, which represents the space-filling properties of the particles, the granular texture may be described in terms of various fabric parameters pertaining to the contact network as the backbone of stress transmission in granular materials. In this section, we use such descriptors in
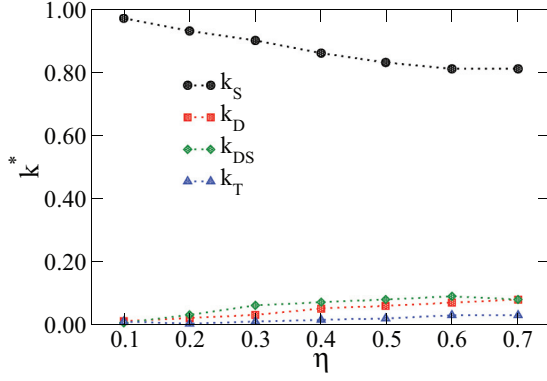
FIG. 21. (Color online) Proportions of simple, double, double-simple, and triple contacts as a function of η in the residual state.

FIG. 23. Coordination number Z^* averaged in the residual state as a function of η. Error bars represent standard deviation.

order to characterize the effect of nonconvexity on the contact network in our cohesive granular packings.

Let us consider the proportions K_S, K_{DS}, K_D, and K_T of simple, double simple, double, and triple contacts, respectively. Given these multiple contacts between aggregates, we also distinguish between the coordination number Z, defined as the mean number of contact neighbors per particle, and the connectivity number Z_c, defined as the mean number of contacts per particle. For disks, these two definitions coincide and we have $Z = Z_c$. But for nonconvex particles, we have $Z < Z_c$ and, thus, the contact network can also be characterized by the ratio $K = Z_c/Z$.

Figure 21 displays these contact type proportions as a function of η in the residual state in our biaxial compression simulations. Simple contacts represent more than 80% of all contacts but it decreases with increasing η and saturates for $\eta > 0.4$. At the same time, the proportions of other contact types are almost equal and they increase with η and saturate like simple contacts. We expected that double contacts should be enhanced in the presence of cohesion between aggregates as they represent strong interlocking. But these contacts do not seem to play a special role in steady shearing.

Figure 22 shows the evolution of Z during shear for different values of η. Z has its highest value in the initial state and it declines fast by contact loss at the beginning of biaxial compression to reach a nearly constant level after 20%
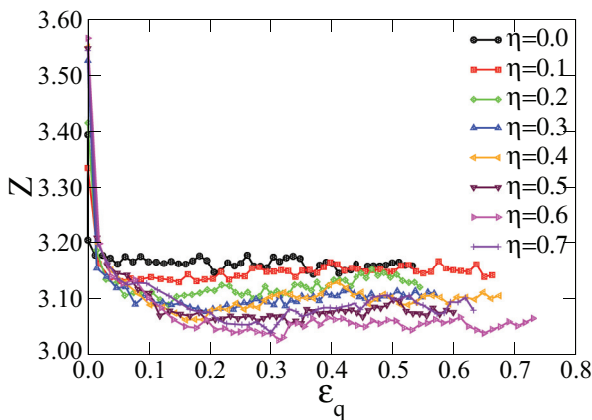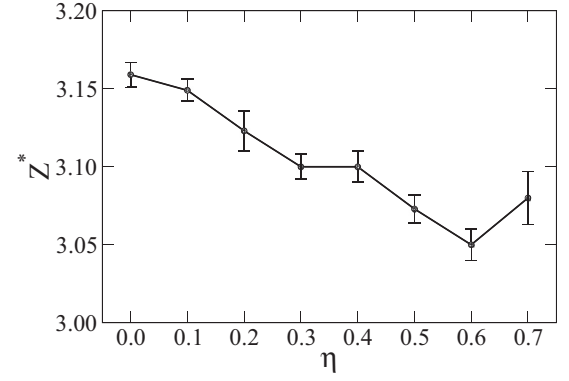
deformation. Figure 23 shows the residual values of Z^* as a function of η. The aggregates which have higher degree of nonconvexity have on average less contact neighbors. It decreases from 3.15 for $\eta = 0.0$ to 3.05 for $\eta = 0.6$. In other words, in steady shearing, the effect of cohesion is to allow for the formation of loose structures with less contact neighbors.

The connectivity number Z_c is shown in Fig. 24. Again, we observe a constant value after a rapid falloff. Figure 25 shows the residual value Z_c^* as a function of η. In contrast to Z^*, here we have an increasing function of η, from 3.15 for $\eta = 0$ to 3.85 for $\eta = 0.7$. This paradoxical evolution of the texture (increasing Z_c^* and decreasing Z^* with η) means that when the degree of nonconvexity increases, the aggregates tend to form more contacts with fewer neighbors. As a result, the parameter K^* in the residual state increases with η as shown in Fig. 26. This observation is in agreement with the simulations of Ludewig *et al.* [45], who found that K during compaction under vibrations increases as the aggregates become rougher.

It is also interesting to distinguish between the partial connectivty numbers Z_c^+ and Z_c^- corresponding to the contacts sustaining compressive and tensile forces, respectively. Figure 27 shows the evolution of Z_c^- and Z_c^+ with shear strain ε_q. Since the packings are initially very dense, both Z_c^- and Z_c^+ decrease rapidly with ε_q by loss of contacts. Then Z_c^+ continues to decrease steadily, whereas Z_c^- increases. This increase of the proportion of tensile contacts indicates the mobilization

FIG. 22. (Color online) Coordination number Z as a function of cumulative shear strain ε_q.
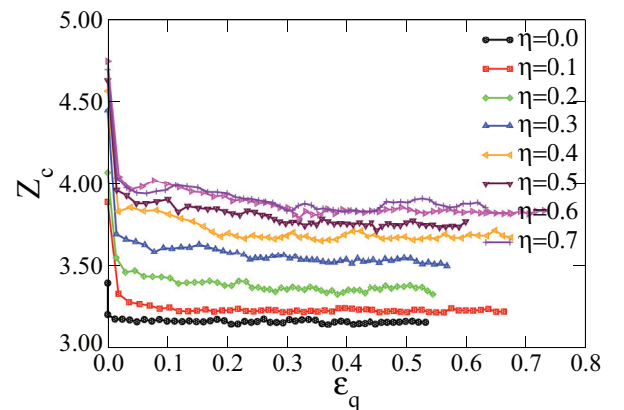

FIG. 24. (Color online) The connectivty number Z_c as a function of cumulative shear stress.
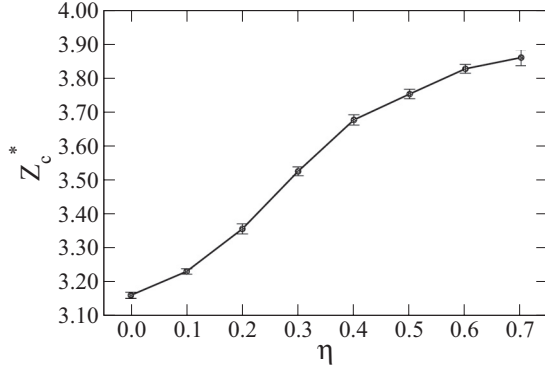
FIG. 25. The connectivity number Z_c^* averaged in the residual state as a function of η. Error bars represent standard deviation.

of adhesion forces along the direction of extension. Hence, a fraction of compressive contacts transforms into tensile contacts. But a nearly constant level is reached at $\varepsilon \simeq 0.3$ for both compressive and tensile contacts.

For all values of η, Z_c^+ is larger than Z_c^-. This is consistent with the fact that in a biaxial compression test the material is globally in a compressive state of stress. We also note that the evolution of Z_c^+ shows less fluctuations than that of Z_c^-. These fluctuations reflect a complex process as the adhesion forces are mobilized in a direction of extension where the stresses are globally compressive. In contrast, the compressive contacts occur mainly in the direction of contraction, which is that of the major principal stress direction.

The cohesive texture can be chatacerized by two dimensionless numbers α and β defined by

$$\alpha = \frac{-\langle f_n^- \rangle}{\langle f_n^+ \rangle + \langle f_n^- \rangle} \tag{9}$$

and

$$\beta = \frac{Z_c^-}{Z_c}. \tag{10}$$

The averages $\langle f_n^- \rangle$ and $\langle f_n^+ \rangle$ represent the mean tensile and compressive normal forces, respectively. We note that $\langle f_n^- \rangle$ is negative, but the sum $\langle f_n^- \rangle + \langle f_n^+ \rangle$ remains positive due the mean compressive stress which is applied on the packings during the shear test. The cohesion of the material may increase
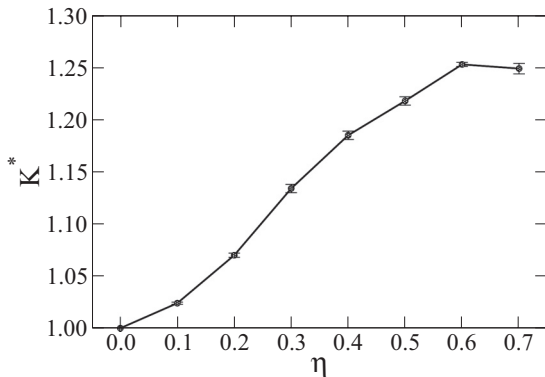
FIG. 26. The ratio K^* of connectivity number to coordination number averaged in the residual state as a function of nonconvexity η. Error bars represent the standard deviation.
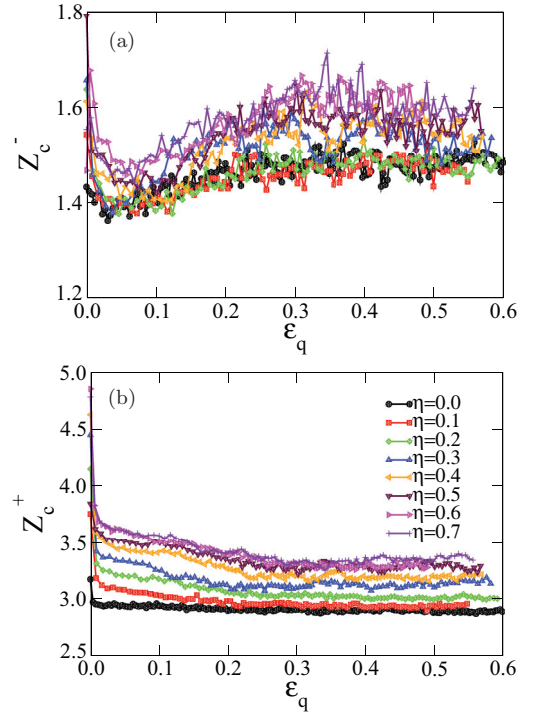
FIG. 27. (Color online) Connectivity numbers Z_c^- and Z_c^+ for tensile (a) and compressive (b) contacts as a function of ε_q for the different values of η.

as a result of the increase of either the proportion of tensile contacts or the magnitude of tensile forces carried by the tensile contacts.

Figure 28 displays the evolution of α and β as a function of ε_q in the biaxial tests with different values of η. In general, α
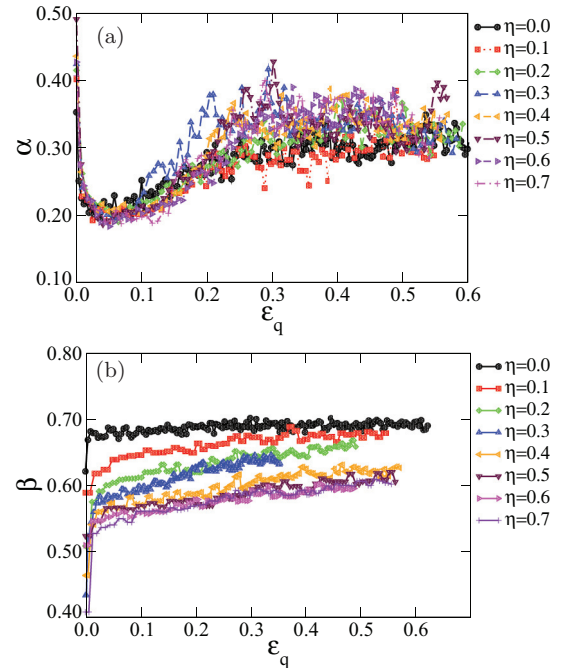
FIG. 28. (Color online) Evolution of the descriptors of the cohesion state α and β with shear strain ε_q for the different values of η.
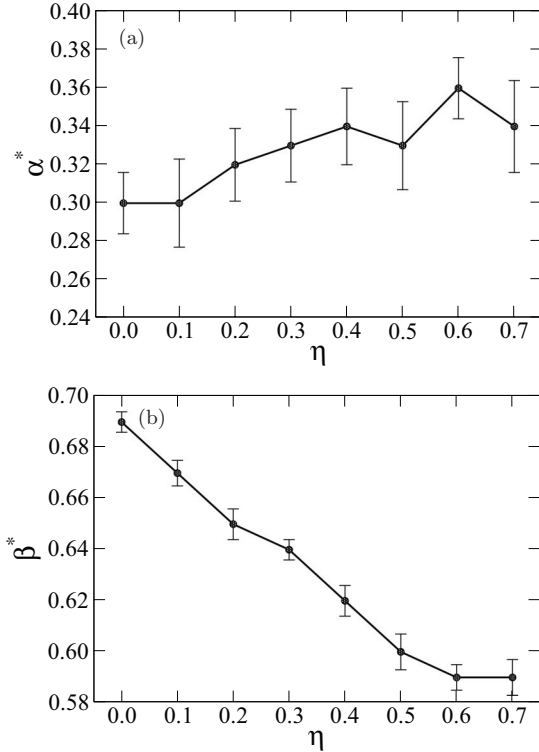
FIG. 29. Descriptors of the cohesion state α^* and β^* in the residual state as a function of η. Error bars represent standard deviation.

FIG. 30. (Color online) Tensile (a) and compressive (b) forces at the beginning of the biaxial shear test for $\eta = 0$. The linewidth is proportional to the normal forces.

has a high value at the beginning of the test. Then, it undergoes a sharp decrease and increases again to move towards a steady value when the system is in the sheared state. On the contrary β is monotonic as a function of ε_q. We observe a sharp increase at the beginning of the test, followed by a slow gradual increase towards the steady state.

Since the cohesive strength of the material involves for both α and β, their opposite variations at the beginning of shear test means that the cohesion increases initially only due to an increasing proportion of tensile contacts although they carry lower tensile forces.

A similar argument holds for the steady-state cohesion as a function of η. Figure 29 shows α^* and β^* in the steady state as a function of η, where we observe an increase of α^* and a decrease of β^* as η increases. This observation implies that the cohesion increases with η only due to an increasing magnitude of tensile forces although their proportion declines. This is again consistent with the fact that higher nonconvexity leads to packing structures with more mobilized cohesive bonds but less bonded particles.

In our discussions about the connectivity of the aggregates, we pointed out the fact that, although the packings are subjected to a compressive state of stress, the tensile contacts occur in the direction of extension, whereas the compressive contacts point mostly in the direction of compression. Figures 30 and 31 display the contact networks separately for tensile and compressive forces at the beginning of the biaxial shear tests for the packings $\eta = 0$ and $\eta = 0.7$. In both cases, the priviledged direction of compressive contacts can be observed with long force chains. But the tensile contacts appear to be
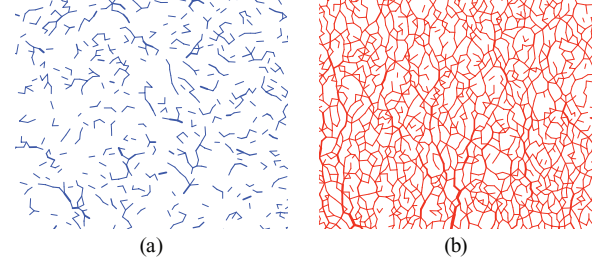
less connected and their orientations less marked than those of compressive contacts.

In order to measure the orientational distribution of the contacts, it is useful to consider the fabric tensor $\boldsymbol{F}$ defined from the contact normals $\vec{n}$ by

$$\boldsymbol{F} = \langle \boldsymbol{n} \otimes \boldsymbol{n} \rangle = \begin{bmatrix} \langle \cos^2 \theta \rangle & \langle \sin \theta \cos \theta \rangle \\ \langle \sin \theta \cos \theta \rangle & \langle \sin^2 \theta \rangle \end{bmatrix}, \quad (11)$$

where $\otimes$ is the dyadic product and the averages are taken over all contacts [70–73]. The anisotropy a_c of the contact network is defined by

$$a_c = 2(F_1 - F_2), \quad (12)$$

where F_1 and F_2 are the principal values of $\boldsymbol{F}$. The major principal direction θ_c of $\boldsymbol{F}$ represents the privileged direction of the contacts.

To follow the anisotropy with shear strain it is useful to consider the "signed" anisotropy a_c' defined by [74]

$$a_c' = 2(F_1 - F_2) \cos 2(\theta_c - \theta'), \quad (13)$$

where θ' is a reference direction, which can be θ_c in the initial state or the major principal direction of the stress tensor. We now define fabric tensors $\boldsymbol{F}^+$ and $\boldsymbol{F}^-$ as in Eq. (11) but with averages restricted to the sets of compressive and tensile contacts, respectively. We also take the reference direction θ' to be that of the major principal stress direction. The corresponding signed anistropies $a_c'^+$ and $a_c'^-$ describe the mean polarization of the two networks.

Figure 32 shows the evolution of $a_c'^+$ and $a_c'^-$ as a function of ε_q for all the values of η. We see that, for all η, $a_c'^+$ increases from 0 (due to the initial isotropic compression), passes by a pronounced peak at $\varepsilon_q \simeq 0.1$, and declines to a contsant value at large strains. At the same time, $a_c'^-$ begins to increase with

FIG. 31. (Color online) Tensile (a) and compressive (b) forces at the beginning of the biaxial shear test for $\eta = 0.7$. The linewidth is proportional to the normal forces.
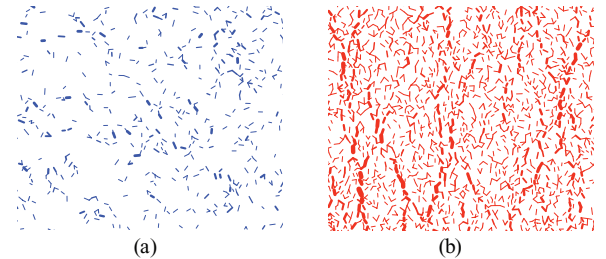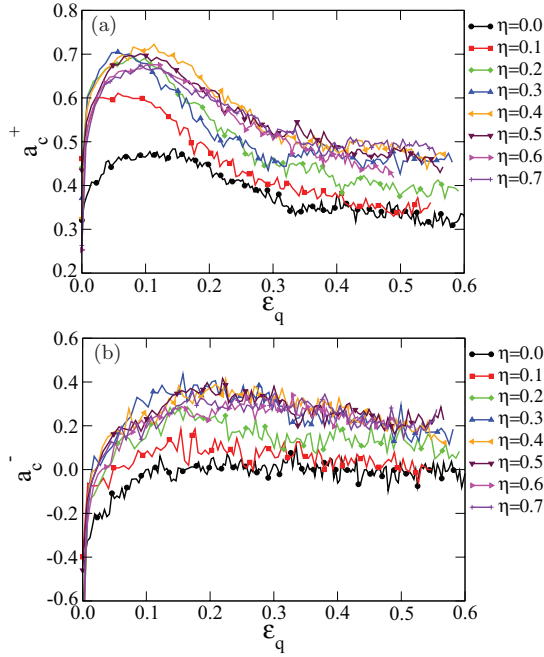
FIG. 32. (Color online) Fabric anisotropy of tensile (a) and compressive (b) contacts as a function of shear strain for different values of η.

FIG. 33. (Color online) Descriptors of the cohesion state α_0 and β_0 at the beginning of simple compression test as a function of η.

low negative values and increases rapidly to become positive at larger strains excepting disk packing and the case $\eta = 0.1$ which tend to an isotropic distribution of tensile contacts. After a peak value reached at $\varepsilon_q \simeq 0.2$, $a_c'^-$ declines but remains positive.

The negative sign of $a_c^{-'}$ means that the average orientation of the tensile contacts is orthogonal to the major principal stress direction (vertical) at low strains. This is consistent with our intuitive image of the mobilization of adhesion forces along the direction of extension. However, the positive values at larger strains contradict this image: In sheared nonconvex packings of aggregates, the tensile contacts tend to be oriented as compressive contacts. Since $a_c^{-'}$ continues to decline with shear strain, it is plausible to assume that it may vanish after longer shearing as in the case of $\eta = 0$ and $\eta = 0.1$. The positive values then may be attributed to the fact that most tensile contacts appear in the shear bands where the local kinematics is different from the global kinematics. In particular, the aggregates tend to rotate by local shearing and the shear bands expand. As more tensile contacts are activated by the evolution of the shear bands and gradual homogenization of the texture, the packing may thus tend to an isotropic state of tensile contact orientations.

In the case of simple compression tests, the initial high value of cohesion reflects the high value of the initial connectivity, which increases with nonconvexity. Figure 33 shows the initial values of α and β (noted α_0 and β_0, respectively) as a function of vertical strain in the case of simple compression tests from the beginning up to the peak stress; see Fig. 13. The observed behaviour is similar to that in the biaxial tests. α_0 drops from a high initial value (higher than in biaxial compression), which reflects the high state of cohesion of the packings. However, the mean values of α_0 and β_0 reached at $\varepsilon_{yy} \simeq 0.03$ both decrease
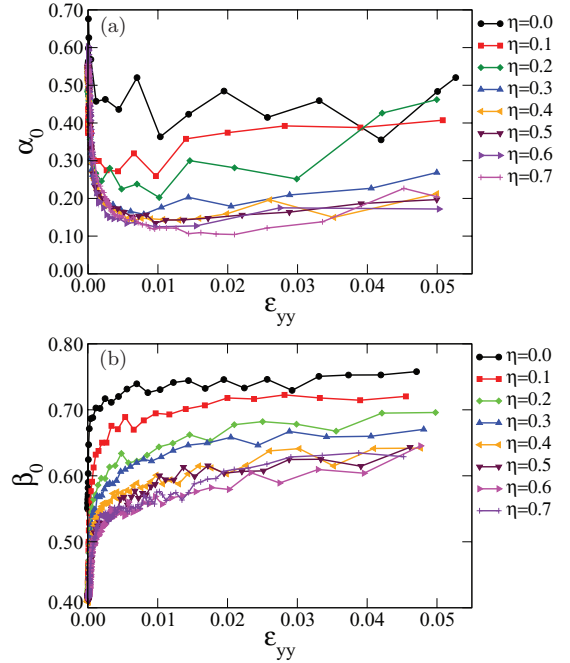
as η increases despite the increase of cohesion as observed in Fig. 14. This shows that α and β do not always reflect the state of cohesion of the packing. The large connectivity allows a packing to resist vertical compression by building up vertical compressive force chains requiring less mobilized adhesion forces as nonconvexity increases.

VI. CONCLUSION

In this paper, we used contact dynamics DEM simulations to investigate the cohesive behavior of 2D packings composed of nonconvex aggregates. The adhesion force between the aggregates was kept constant, whereas the nonconvexity was varied in a broad range. The contact adhesion upscales to a macroscopic cohesion which is expected to be amplified by interlocking effect induced by shape nonconvexity. It was shown, however, that the macroscopic cohesion evaluated from the Mohr-Coulomb criterion is sensibly dependent on the boundary conditions. Even with homogeneous loading, the packings develop strain inhomogeneities in the form of shear bands and/or stress inhomogeneities in the form of gradients due to the mobilization of friction forces at the walls. Therefore, the tensile forces are not homogeneously mobilized within the packings and the resulting cohesion does not reflect an intrinsic material property but represents a cohesion state which either fluctuates with nonconvexity or remains far below the expected cohesion. For example, the cohesion levels measured in simple compression tests were found to be one order of magnitude above those in biaxial compression tests. The largest cohesion was found at the beginning of unconfined compression test where the sample is homogeneously deformed without showing stress and strain gradients. In this case, the macroscopic cohesion is a linear function of nonconvexity. In order to get more insight into the

particle-scale mechanisms of cohesion and its evolution, we analyzed the local packing fractions and textures in terms of connectivity and anisotropy. A nontrivial observation is that, as the nonconvexity increases, the coordination number (number of contact neighbors) declines, whereas the connectivity number (number of contacts) increases. In other words, the aggregates tend to make more contacts with less contact neighbors. Moreover, we found that the compressive contacts always point along the direction of compression, whereas the tensile contacts in sheared packings have either an isotropic distribution or follow the direction of compression. It was argued that this behavior relates to the local kinematics within the shear band and the incomplete mobilization of adhesion forces elsewhere. In order to handle more realistic model, an interesting issue for this work could be to introduce adhesive forces that depend of the particles local radius of curvature. Analytical model such as that introduced in Ref. [75] could be a interesting perspective.

Further simulations are required to test other boundary conditions. For example, a major issue in many applications is whether uniaxial compression (oedometric test) may erase the inhomogeneities in packing fraction. Simulations are underway to investigate this issue and the general compaction properties of nonconvex particles with and without cohesion.

APPENDIX: CONTACT DYNAMICS METHOD

In this Appendix, we briefly describe the contact dynamics (CD) method in 2D by adapting a detailed description given in Ref. [56]. The implementation of the CD method with adhesion forces is given in Sec. II.

1. Contact laws

Let us consider two particles i and j with a contact at a point κ within a granular material. We assume that a unique common line (plane in 3D) tangent to the two particles at κ can be geometrically defined so the contact can be endowed with a local reference frame defined by a unit vector $\vec{n}$ normal to the common line and a unit vector $\vec{t}$ along the tangent line with an appropriate choice of the orientations of the axes.

Geometrically, a contact potentially exists if the gap δ_n between two particles is so small that within a small time interval δt (time step in numerical simulations) a collision may occur between the two particles. If the contact is effective, i.e., for $\delta_n = 0$, a repulsive (positive) normal force f_n may appear at κ with a value depending on the particle velocities and contact forces acting on the two partners by their neighboring particles; see Fig. 34. But if δ_n is positive (a gap), the potential contact is not effective and f_n at the potential contact κ is identically zero. These disjunctive conditions can be described by the following inequalities:

$$\delta_n > 0 \Rightarrow f_n = 0$$
$$\delta_n = 0 \Rightarrow f_n \geqslant 0. \tag{A1}$$

The important point about this relation between δ_n and f_n, called Signorini's conditions, is that it cannot be reduced to a (mono-valued) function. Signorini's conditions imply that the normal force vanishes when the contact is not effective. But the normal force may vanish also at an effective contact. In
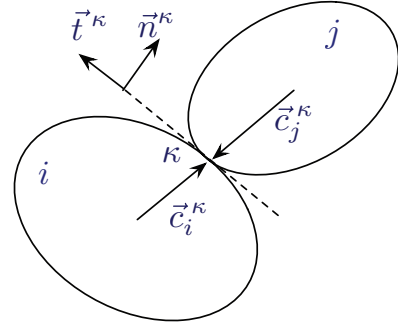

FIG. 34. (Color online) Geometry of a contact κ between two particles i and j with contact vectors $\vec{c}_i^{\kappa}$ and $\vec{c}_j^{\kappa}$, and contact frame $(\vec{n}^{\kappa}, \vec{t}^{\kappa})$.

particular, this is the case for $u_n = \dot{\delta}_n > 0$, i.e., for incipient contact opening. Otherwise, the effective contact is *persistent* and we have $u_n = \dot{\delta}_n = 0$. Hence, Signorini's conditions can be split as follows:

$$\delta_n > 0 \Rightarrow f_n = 0$$
$$\delta_n = 0 \ \wedge \ \begin{cases} u_n > 0 \Rightarrow f_n = 0 \\ u_n = 0 \Rightarrow f_n \geqslant 0. \end{cases} \tag{A2}$$

We see that for an effective contact, i.e., for $\delta_n = 0$, Signorini's conditions hold between the variables u_n and f_n.

Like Signorini's conditions, the Coulomb law of dry friction at an effective contact point can be expressed by a set of alternative inequalities for the friction force f_t and the sliding velocity u_t,

$$u_t > 0 \Rightarrow f_t = -\mu f_n$$
$$u_t = 0 \Rightarrow -\mu f_n \leqslant f_t \leqslant \mu f_n \tag{A3}$$
$$u_t < 0 \Rightarrow f_t = \mu f_n,$$

where μ is the coefficient of friction and it is assumed that the unit tangent vector $\boldsymbol{t}$ points in the direction of the sliding velocity so $\vec{u}_t \cdot \vec{t} = u_t$. Like Signorini's conditions, this is a degenerate law that cannot be reduced to a (mono-valued) function between u_t and f_t.

Signorini's conditions (A2) and Coulomb's friction law (A3) are represented as two graphs in Fig. 35 for an effective contact between two particles. We refer to these graphs as *contact laws* in the sense that they characterize the relation between relative displacements and forces irrespective of the material behavior (viscoelastic or plastic nature) of the particles. These contact laws should be contrasted with *force laws* (employed in MD simulations), which describe a functional depedence between elastic or plastic deflections
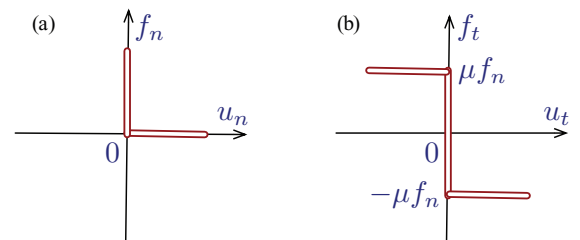

FIG. 35. (Color online) Graphs of (a) Signorini's conditions and (b) Coulomb's friction law.

(attributed to the contact point) and forces extracted from the material behavior of the particles. The force laws often employed in MD may also be considered as a "regularization" of the contact laws, in which the vertical branches in Signorini's and Coulomb's graphs are replaced by a steep linear or nonlinear function.

2. Augmented contact laws

The use of contact laws in the CD method is consistent with the idea of a discrete model defined only at the scale of particle motions and involving no small subparticle length or force scales inherent to the force laws. But such a "coarse-time" model of particle motion implies *nonsmooth dynamics*, i.e., possible discontinuities in particle velocities and forces arising from collisions and variations of the contact status (effective or not, persistent or not, sliding or not). Such *events* occur frequently in granular flows and, hence, the approximation of the contact force f_n during δt is a *measure* problem in the mathematical sense [49,76]. A static or regular force f^s is the density of the measure $f^s\,dt$ with respect to time differential dt. In contrast, an impulse p generated by a collision has no density with respect to dt. In other words, the forces at the origin of the impulse are not resolved at the scale δt. In practice, however, we cannot differentiate between these contributions in a "coarse-time" dynamics, and the two contributions should be summed up to a single measure. The contact force then is defined as the average of this measure over δt.

In a similar vein, the left-limit velocities u_n^- and u_t^- at time t are not always related by a smooth variation (acceleration multiplied by the time step δt) with the right-limit velocities u_n^+ and u_t^+ at $t + \delta t$. Hence, we assume that the contact laws (A2) and (A3) are satisfied for a weighted mean of the relative left-limit and right-limit velocities,

$$u_n = \frac{u_n^+ + e_n\, u_n^-}{1 + e_n}, \qquad (A4)$$

$$u_t = \frac{u_t^+ + e_t\, u_t^-}{1 + |e_t|}. \qquad (A5)$$

The physical meaning of the coefficients e_n and e_t is best illustrated by considering a binary collision between two particles. A binary collision corresponds to an effective contact occuring in the interval $[t, t + \delta t]$ and a persistent contact in the sense of the mean velocity u_n. In other words, we have $u_n = 0$ and, thus, $-u_n^+/u_n^- = e_n$. Hence, e_n may be identified with the normal restitution coefficient. In the same way, for $u_t = 0$, corresponding to a nonsliding condition (adherence of the two particles during their contact), implies $-u_t^+/u_t^- = e_t$, which is the tangential restitution coefficient. We see that when Signorini's and Coulomb's graphs are used with the mean velocities given by Eq. (A12), a contact is persistent in terms of u_n^+ (i.e., $u_n^+ = 0$) only if $e_n = 0$.

When a collision is not binay, the generated impulses propagate through the contact network so a contact may experience several successive impulses during δt. Such events can be resolved for a sufficiently small time increment δt or they may be tracked according to an event-driven scheme. The event-tracking strategy is, however, numerically inefficient, of limited applicability and in contradiction with the scope of the CD method based on coarse-time dynamics. The use

of mean velocities (A12) with the contact laws, thus should be considered a generalization of restitution coefficients to multiple collisions and contact networks for which the right-limit veocities u_n^+ and u_t^+ are not simply given by the left-limit velocities multiplied by the coefficients of restitution as in binary collisions but by combining the contact laws with the equations of dynamics.

3. Nonsmooth motion

The rigid-body motion of the particles is governed by Newton's equations under the action of imposed external bulk or boundary forces $\vec{F}_{\text{ext}}$, and the contact reaction forces $\vec{f}^\kappa$ exerted by neighboring particles at the contact points κ. An absolute reference frame with unit vectors $(\hat{x}, \hat{y})$ is assumed, and we set $\hat{z} = \hat{x} \times \hat{y}$. Each particle is characterized by its mass m, moment of inertia I, mass center coordinates $\vec{r}$, mass center velocity $\vec{U}$, angular coordinates θ, and angular velocity $\omega\hat{z}$. For a smooth motion (twice differentiable), the equations of motion of a particle are

$$\begin{aligned} m\,\dot{\vec{U}} &= \vec{F} + \vec{F}_{\text{ext}} \\ I\,\dot{\omega} &= \mathcal{M} + \mathcal{M}_{\text{ext}}, \end{aligned} \qquad (A6)$$

where $\vec{F} = \sum_\kappa \vec{f}^\kappa$ and $\mathcal{M} = \hat{z} \cdot \sum_\kappa \vec{c}^\kappa \times \vec{f}^\kappa$, where $\vec{c}^\kappa$ is the *contact vector* joining the center of mass to the contact κ and $\mathcal{M}_{\text{ext}}$ represents the moment of external forces.

For a nonsmooth motion with time resolution δt involving impulses and velocity discontinuities, an integrated form of the equations of dynamics should be used. Hence, the equations of dynamics should be written as an equality of measures,

$$\begin{aligned} m\,d\vec{U} &= d\vec{F}' + \vec{F}_{\text{ext}}\,dt \\ I\,d\omega &= d\mathcal{M}' + \mathcal{M}_{\text{ext}}\,dt, \end{aligned} \qquad (A7)$$

where $d\vec{F}' = \sum_\kappa d\vec{f}'^\kappa$ and $d\mathcal{M}' = \hat{z} \cdot \sum_\kappa \vec{c}^\kappa \times d\vec{f}'^\kappa$. These measure differential equations can be integrated over δt with the definitions of $\vec{F}$ and $\mathcal{M}$ as approximations of the integral of $d\vec{F}'$ and $d\mathcal{M}'$. With these definitions, the integration of equation (A7) over δt yields

$$\begin{aligned} m\,(\vec{U}^+ - \vec{U}^-) &= \delta t\,\vec{F} + \delta t\,\vec{F}_{\text{ext}} \\ I\,(\omega^+ - \omega^-) &= \delta t\,\mathcal{M} + \delta t\,\mathcal{M}_{\text{ext}}, \end{aligned} \qquad (A8)$$

where $(\vec{U}^-, \omega^-)$ and $(\vec{U}^+, \omega^+)$ are the left-limit and right-limit velocities of the particle, respectively.

The equations of dynamics can be written in a compact form for a set of N_p particles by using matrix representation. The particles are labeled with integers $i \in [1, N_p]$. The forces and force moments $F_x^i, F_y^i, \mathcal{M}^i$ acting on the particles i are arranged in a single high-dimensional column vector represented by a bold letter $\boldsymbol{F}$ belonging to $\mathbb{R}^{3N_p}$. In the same way, the external bulk forces $F_{\text{ext},x}, F_{\text{ext},y}, \mathcal{M}_{\text{ext}}$ applied on the particles and the particle velocity components U_x^i, U_y^i, ω^i are represented by column vectors $\boldsymbol{F}_{\text{ext}}$ and $\boldsymbol{U}$, respectively. The particle masses and moments of inertia define a diagonal $3N_p \times 3N_p$ matrix denoted by $\boldsymbol{M}$. With these notations, the equations of dynamics (A8) are cast into a single matrix equation,

$$\boldsymbol{M}(\boldsymbol{U}^+ - \boldsymbol{U}^-) = \delta t (\boldsymbol{F} + \boldsymbol{F}_{\text{ext}}). \qquad (A9)$$

4. Contact dynamics equations

Since the contact laws are expressed in contact variables (u_n, u_t, f_n, and f_t), we need to express the equations (A9) in the same variables. The contacts are labeled with integers $\kappa \in [1, N_c]$, where N_c is the total number of contacts. Like particle velocities, the contact velocities u_n^κ and u_t^κ can be collected in a column vector $\boldsymbol{u} \in \mathbb{R}^{2N_c}$. In the same way, the contact forces f_n^κ and f_t^κ are represented by a vector $\boldsymbol{f} \in \mathbb{R}^{2N_c}$. We would like to transform the equations of dynamics from $\boldsymbol{F}$ and $\boldsymbol{U}$ to $\boldsymbol{f}$ and $\boldsymbol{u}$. The formal transformation of matrix equations (A9) is straightforward. Since the contact velocities $\boldsymbol{u}$ are linear in particle velocities $\boldsymbol{U}$, the transformation of the velocities is an affine application,

$$\boldsymbol{u} = \boldsymbol{G}\,\boldsymbol{U}, \tag{A10}$$

where $\boldsymbol{G}$ is a $2N_c \times 3N_p$ matrix containing basically information about the geometry of the contact network. A similar linear application relates $\boldsymbol{f}$ to $\boldsymbol{F}$,

$$\boldsymbol{F} = \boldsymbol{H}\,\boldsymbol{f}, \tag{A11}$$

where $\boldsymbol{H}$ is a $3N_p \times 2N_c$ matrix. We refer to $\boldsymbol{H}$ as a *contact matrix*. It contains the same information as $\boldsymbol{G}$ in a dual or symmetric manner. It can be shown that $\boldsymbol{H} = \boldsymbol{G}^T$, where $\boldsymbol{G}^T$ is the transpose of $\boldsymbol{G}$. This property can be inferred from the equivalence between the virtual power $\boldsymbol{F} \cdot \boldsymbol{U}$ developed by "generalized" forces $\boldsymbol{F}$ and the virtual power $\boldsymbol{f} \cdot \boldsymbol{u}$ developed by the bond forces $\boldsymbol{f}$. In general, the matrix $\boldsymbol{H}$ is singular and, by definition, its null space has a dimension at least equal to $2N_c - 3N_p$.

The matrix $H^{i\kappa}$ can be decomposed into two matrices $H_n^{i\kappa}$ and $H_t^{i\kappa}$ such that

$$
\begin{aligned}
u_n^\kappa &= \sum_i H_n^{T,\kappa i}\,U^i \\
u_t^\kappa &= \sum_i H_t^{T,\kappa i}\,U^i
\end{aligned}
\tag{A12}
$$

and

$$F^i = \sum_\kappa \left(H_n^{i\kappa} f_n^\kappa + H_t^{i\kappa} f_t^\kappa \right). \tag{A13}$$

Using these relations, the Eqs. (A9) can be transformed into two equations for each contact κ,

$$
\begin{aligned}
u_n^{\kappa+} - u_n^{\kappa-} &= \delta t \sum_{i,j} H_n^{T,\kappa i}\, M^{-1,ij} \\
&\quad \times \left\{ \sum_\lambda \left(H_n^{j\lambda} f_n^\lambda + H_t^{j\lambda} f_t^\lambda \right) + F_{\text{ext}}^j \right\}, \\
u_t^{\kappa+} - u_t^{\kappa-} &= \delta t \sum_{i,j} H_t^{T,\kappa i}\, M^{-1,ij} \\
&\quad \times \left\{ \sum_\lambda \left(H_n^{j\lambda} f_n^\lambda + H_t^{j\lambda} f_t^\lambda \right) + F_{\text{ext}}^j \right\}.
\end{aligned}
\tag{A14}
$$

We now can make appear explicitly linear relations between the contact variables from Eqs. (A14) and definitions (A12). Let us set

$$\mathcal{W}_{k_1 k_2}^{\kappa\lambda} = \sum_{i,j} H_{k_1}^{T,\kappa i}\, M^{-1,ij}\, H_{k_2}^{j\lambda}, \tag{A15}$$

where k_1 and k_2 stand for n or t. With this notation, Eqs. (A14) can be rewritten as follows:

$$
\begin{aligned}
\frac{1+e_n}{\delta t}\left(u_n^\kappa - u_n^{\kappa-}\right) &= \mathcal{W}_{nn}^{\kappa\kappa} f_n^\kappa + \mathcal{W}_{nt}^{\kappa\kappa} f_t^\kappa \\
&\quad + \sum_{\lambda(\neq\kappa)} \left\{ \mathcal{W}_{nn}^{\kappa\lambda} f_n^\lambda + \mathcal{W}_{nt}^{\kappa\lambda} f_t^\lambda \right\} \\
&\quad + \sum_{i,j} H_n^{T,\kappa i}\, M^{-1,ij}\, F_{\text{ext}}^j.
\end{aligned}
\tag{A16}
$$

$$
\begin{aligned}
\frac{1+e_t}{\delta t}\left(u_t^\kappa - u_t^{\kappa-}\right) &= \mathcal{W}_{tn}^{\kappa\kappa} f_n^\kappa + \mathcal{W}_{tt}^{\kappa\kappa} f_t^\kappa \\
&\quad + \sum_{\lambda(\neq\kappa)} \left\{ \mathcal{W}_{tn}^{\kappa\lambda} f_n^\lambda + \mathcal{W}_{nt}^{\kappa\lambda} f_t^\lambda \right\} \\
&\quad + \sum_{i,j} H_t^{T,\kappa i}\, M^{-1,ij}\, F_{\text{ext}}^j.
\end{aligned}
\tag{A17}
$$

The coefficients $\mathcal{W}_{k_1 k_2}^{\kappa\kappa}$ for each contact κ can be calculated as a function of the contact network geometry and inertia parameters of the two partners 1_κ and 2_κ of the contact κ. Let $\vec{c}_i^\kappa$ be the *contact vector* joining the center of mass of particle i to the contact κ. We get

$$
\begin{aligned}
\mathcal{W}_{nn}^{\kappa\kappa} &= \frac{1}{m_{1_\kappa}} + \frac{1}{m_{2_\kappa}} + \frac{\left(c_{1t}^\kappa\right)^2}{I_{1_\kappa}} + \frac{\left(c_{2t}^\kappa\right)^2}{I_{2_\kappa}}, \\
\mathcal{W}_{tt}^{\kappa\kappa} &= \frac{1}{m_{1_\kappa}} + \frac{1}{m_{2_\kappa}} + \frac{\left(c_{1n}^\kappa\right)^2}{I_{1_\kappa}} + \frac{\left(c_{2n}^\kappa\right)^2}{I_{2_\kappa}}, \\
\mathcal{W}_{nt}^{\kappa\kappa} &= \mathcal{W}_{tn}^{\kappa\kappa} = \frac{c_{1n}^\kappa c_{1t}^\kappa}{I_{1_\kappa}} + \frac{c_{2n}^\kappa c_{2t}^\kappa}{I_{2_\kappa}},
\end{aligned}
\tag{A18}
$$

where $c_{in}^\kappa = \vec{c}_i^\kappa \cdot \vec{n}^\kappa$ and $c_{it}^\kappa = \vec{c}_i^\kappa \cdot \vec{t}^\kappa$ are the components of the contact vectors in the contact frame. The coefficients $\mathcal{W}_{k_1 k_2}^{\kappa\kappa}$ are inverse reduced inertia.

An alternative representation of Eqs. (A16) and (A17) is the following:

$$\mathcal{W}_{nn}^{\kappa\kappa} f_n^\kappa + \mathcal{W}_{nt}^{\kappa\kappa} f_t^\kappa = (1+e_n)\frac{1}{\delta t}u_n^\kappa + a_n^\kappa, \tag{A19}$$

$$\mathcal{W}_{tt}^{\kappa\kappa} f_t^\kappa + \mathcal{W}_{tn}^{\kappa\kappa} f_n^\kappa = (1+e_t)\frac{1}{\delta t}u_t^\kappa + a_t^\kappa. \tag{A20}$$

The two offsets a_n^κ and a_t^κ can easily be expressed from Eqs. (A16) and (A17). Equations (A19) and (A20) or, equivalently, Eqs. (A16) and (A17) are *contact dynamics equations* as they replace the equations of dynamics of the system in terms of contact variables [56]. The two terms a_n and a_t are given by the following expressions:

$$a_n^\kappa = b_n^\kappa - (1+e_n)\frac{1}{\delta t}u_n^{\kappa-} + \left(\frac{\vec{F}_{\text{ext}}^{2_\kappa}}{m_{2_\kappa}} - \frac{\vec{F}_{\text{ext}}^{1_\kappa}}{m_{1_\kappa}}\right) \cdot \vec{n}^\kappa. \tag{A21}$$

$$a_t^\kappa = b_t^\kappa - (1+e_t)\frac{1}{\delta t}u_t^{\kappa-} + \left(\frac{\vec{F}_{\text{ext}}^{2_\kappa}}{m_{2_\kappa}} - \frac{\vec{F}_{\text{ext}}^{1_\kappa}}{m_{1_\kappa}}\right) \cdot \vec{t}^\kappa. \tag{A22}$$

The effect of left-limit velocities ($u_n^{\kappa-}, u_t^{\kappa-}$) appears in these equations as an impulse depending on the reduced mass and the restitution coefficient. The effect of contact forces $\vec{f}_i^\lambda$ acting on the two touching particles are represented by the terms b_n^κ and b_t^κ given by

$$b_n^\kappa = \frac{1}{m_{2_\kappa}} \sum_{\lambda(\neq\kappa)} \vec{f}_{2_\kappa}^\lambda \cdot \vec{n}^\kappa - \frac{1}{m_{1_\kappa}} \sum_{\lambda(\neq\kappa)} \vec{f}_{1_\kappa}^\lambda \cdot \vec{n}^\kappa, \tag{A23}$$
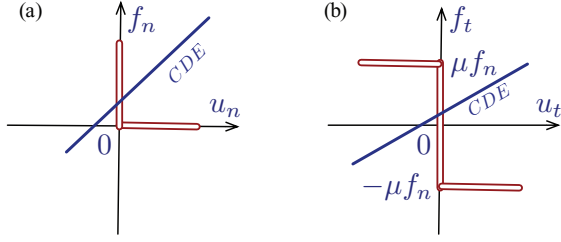
FIG. 36. (Color online) Solution of the local Signorini-Coulomb problem at the intersection points between contact dynamics equations (CDE) and contact laws.

$$b_t^\kappa = \frac{1}{m_{2_\kappa}} \sum_{\lambda(\neq\kappa)} \vec{f}_{2_\kappa}^\lambda \cdot \vec{t}^\kappa - \frac{1}{m_{1_\kappa}} \sum_{\lambda(\neq\kappa)} \vec{f}_{1_\kappa}^\lambda \cdot \vec{t}^\kappa. \qquad (A24)$$

The contact dynamics equations (A19) and (A20) define a system of two linear equations between the contact variables at each contact point. The solution, when the values of a_n and a_t at a contact are assumed, should also verify the contact laws (A2) and (A3). Graphically, this means that the solution is at the intersection between the straight line (A19) and Signorini's graph, on one hand, and between (A20) and Coulomb's graph, on the other hand.

5. Iterative resolution

In order to solve the system of $2N_c$ contact dynamics equations (in 2D) with the corresponding contact laws, we proceed by an iterative method which converges to the solution simultaneously for all contact forces and velocities. We first consider a single-contact problem which consists of the determination of contact variables f_n^κ, f_t^κ, u_n^κ, and u_t^κ at a single contact given the values of the offsets a_n^κ and a_t^κ at the same contact. The solution is given by intersecting the lines representing contact dynamics equations with Signorini's and Coulomb's graphs; see Fig. 36. The intersection occurs at a unique point due to the positivity of the coefficients $\mathcal{W}_{k_1k_2}^{\kappa\kappa}$ (positive slope).

Notice, however, that the two intersections cannot be established separately when $\mathcal{W}_{nt}^{\kappa\kappa} \neq 0$. To find the local solution, one may consider the intersection of contact dynamics equations with the force axis, i.e., by setting $u_n = u_t = 0$. This yields two values g_n^κ and g_t^κ of f_n^κ and f_t^κ, respectively,

$$g_n^\kappa = \frac{\mathcal{W}_{tt}^{\kappa\kappa} a_n^\kappa - \mathcal{W}_{nt}^{\kappa\kappa} a_t^\kappa}{\mathcal{W}_{nn}^{\kappa\kappa}\mathcal{W}_{tt}^{\kappa\kappa} - (\mathcal{W}_{nt}^{\kappa\kappa})^2}, \qquad (A25)$$

$$g_t^\kappa = \frac{\mathcal{W}_{nn}^{\kappa\kappa} a_n^\kappa - \mathcal{W}_{tn}^{\kappa\kappa} a_t^\kappa}{\mathcal{W}_{tt}^{\kappa\kappa}\mathcal{W}_{nn}^{\kappa\kappa} - (\mathcal{W}_{tn}^{\kappa\kappa})^2}. \qquad (A26)$$

It can be shown that the denominator is positive. If $g_n^\kappa < 0$, then the solution is $f_n^\kappa = f_t^\kappa = 0$. This corresponds to a breaking contact. Otherwise, i.e., if $g_n^\kappa \geqslant 0$, we have $f_n^\kappa = g_n^\kappa$. With this value of f_n^κ, we can determine the solution of the Coulomb problem. If $g_t^\kappa > \mu f_n^\kappa$, the solution is $f_t^\kappa = \mu f_n^\kappa$ and in the opposite case, i.e., if $g_t^\kappa < -\mu f_n^\kappa$, the solution is $f_t^\kappa = -\mu f_n^\kappa$ (sliding contact). Otherwise, i.e., when $-\mu f_n^\kappa < g_t^\kappa < \mu f_n^\kappa$, the solution is $f_t^\kappa = g_t^\kappa$ (rolling contact).

In a multicontact system, the terms b_n^κ and b_t^κ in the offsets a_n^κ and a_t^κ depend on the forces and velocities at contacts

$\lambda \neq \kappa$; see Eqs. (A21), (A21), (A23), and (A24). Hence, the solution for each contact depends on all other contacts of the system and it must be determined simultaneously for all contacts. An intuitive and robust method to solve the system is to search the solution as the limit of a sequence $\{f_n^\kappa(k), f_t^\kappa(k), u_n^\kappa(k), u_t^\kappa(k)\}$ with $\kappa \in [1, N_c]$. Let us assume that the transient set of contact forces $\{f_n^\kappa(k), f_t^\kappa(k)\}$ at iteration step k is given. From this set, the offsets $\{a_n^\kappa(k), a_t^\kappa(k)\}$ for all contacts can be calculated through the relations (A21) and (A22). The local problem can then be solved for each contact κ with these values of the offsets, yielding an updated set of contact forces $\{f_n^\kappa(k+1), f_t^\kappa(k+1)\}$.

Remark that this force update procedure does not require the contact velocities $u_n^\kappa(k+1), u_t^\kappa(k+1)\}$ to be calculated since the offsets depend only on the contact forces. The set $\{f_n^\kappa(k), f_t^\kappa(k)\}$ evolves with k by successive corrections and it converges to a solution satisfying the contact dynamics equations and contact laws at all potential contacts of the system. The iterations can be stopped when the set $\{f_n^\kappa(k), f_t^\kappa(k)\}$ is stable with regard to the force update procedure within a prescribed precision criterion ε_f,

$$\frac{|f^\kappa(k+1) - f^\kappa(k)|}{f^\kappa(k+1)} < \varepsilon_f \quad \forall\kappa. \qquad (A27)$$

Finally, from the converged contact forces, the particle velocities $\{\vec{U}^i\}$ can be computed by means of the equations of dynamics (A8).

The iterative procedure depicted above provides a robust method which proves efficient in the context of granular dynamics. The information is treated locally and no large matrices are manipulated during iterations. The number N_i of necessary iterations to converge is strongly dependent on the precision ε_f but not on δt. The number of iterations is substantially reduced when the iteration is initialized with a globally correct guess of the forces. This is the case when the forces at each time step are initialized with the forces computed in the preceding step.

The uniqueness of the solution in a multicontact system with rigid particles is not guranteed at each step of evolution. We have $3N_p$ equations of dynamics and $2N_c$ contact relations. The unknowns of the problem are $3N_p$ particle velocities and $2N_c$ contact forces. The indeterminacy arises from the fact that the $2N_c$ contact relations are *inequations*. Thus, the extent of indeterminacy of the solution reflects all possible combinations of contact forces accommodating the contact inequations. The degree of indeterminacy may be high, but it does not imply significant force variability since the solutions are strongly restrained by the contact laws. In practice, as a result of finite numerical precision, the risk of not finding a mechanically admissible solution (verifying the contact laws and equations of dynamics) is higher than that of finding too many solutions. In other words, the variability of the solution is often below the precision controlled by ε_f when the forces are computed at each time step from the forces at the preceding step.

6. Time-stepping scheme

In CD method, the global problem of the determination of forces and velocities, as described above, is associated with a time-stepping scheme. This scheme is based on the fact that

the first condition of Signorini's relations in (A2) is the only condition referring to space coordinates. Both the equations of dynamics and contact laws are formulated at the velocity level, and the first condition of Signorini is accounted for by considering only the *effective contacts* where $\delta_n = 0$. Hence, the contact network is defined explicitly from particle positions and it does not evolve during the time interval δt. But the treatment of forces and velocities is fully *implicit*, and the right-limit velocities $\{\vec{U}^{i+}, \omega^{i+}\}$ should be used to increment particle positions.

These remarks devise the following time-stepping scheme. Let t and $t + \delta t$ be the considered time interval. The configuration $\{\vec{r}^i(t)\}$ and particle velocities $\{\vec{U}^i(t), \omega^i(t)\}$ are given at time t. The latter play the role of left-limit velocities $\{\vec{U}^{i-}, \omega^{i-}\}$. The contact network $\{\kappa, \vec{n}^\kappa, \vec{t}^\kappa\}$ is set up from the configuration at time t or from an intermediate configuration $\{\vec{r}_m^i\}$ defined by

$$\vec{r}_m^i \equiv \vec{r}^i(t) + \frac{\delta t}{2} \vec{U}^i(t). \tag{A28}$$

When this configuration is used for contact detection, other space-dependent quantities such as the inverse mass parameters $\mathcal{W}_{k_1 k_2}^{\kappa \kappa}$ and external forces $\vec{U}_{\text{ext}}^i$ should consistently be defined for the same configuration and at the same time $t + \delta t/2$. The forces and velocities then are iteratively determined for the contact network, and the right-limit particle velocities $\{\vec{U}^{i+}, \omega^{i+}\}$ are calculated. The latter correspond to the velocities at the end of the time step $t + \delta t$,

$$\vec{U}^i(t + \delta t) = \vec{U}^{i+}, \tag{A29}$$

$$\omega^i(t + \delta t) = \omega^{i+}. \tag{A30}$$

Finally, the positions are updated by integrating the updated velocities,

$$\vec{r}^i(t + \delta t) = \vec{r}_m^i + \frac{\delta t}{2} \vec{U}^i(t + \delta t), \tag{A31}$$

$$\theta^i(t + \delta t) = \theta_m^i + \frac{\delta t}{2} \omega^i(t + \delta t). \tag{A32}$$

This scheme is unconditionally stable due to its inherent implicit time integration. Hence, no damping parameters at any level are needed. For this reason, the time step δt can be large. The real limit imposed on the time step is cumulative round-off errors in particle positions, which are updated from the integration of the velocities. Although the excessive overlaps have no dynamic effect in the CD method, they falsify the geometry and, thus, the evolution of the system. A sufficiently high precision or a large enough number of iterations is required to avoid such errors. The time step is not a precision parameter but a coarse-graining parameter for nonsmooth dynamics. It should be reduced if the impulse dynamics at small time scales is of interest.

---

[1] R. M. Nedderman, *Statics and Kinematics of Granular Materials* (Cambridge University Press, Cambridge, 1992).

[2] F. Radjai, I. Preechawuttipong, and R. Peyroux, in *Continuous and Discontinuous Modeling of Cohesive Frictional Materials*, edited by P. Vermeer, S. Diebels, W. Ehlers, H. Herrmann, S. Luding, and E. Ramm (Springer Verlag, Berlin, 2001), pp. 148–159.

[3] F. A. Gilabert, J.-N. Roux, and A. Castellanos, Phys. Rev. E **78**, 031305 (2008).

[4] J. Fourcade, P. Sornay, F. Sudreau, and P. Papet, Powder Metall. **49**, 125 (2006).

[5] R. Y. Yang, R. P. Zou, and A. B. Yu, Phys. Rev. E **62**, 3900 (2000).

[6] D. Kadau, G. Bartels, L. Brendel, and D. E. Wolf, Comput. Phys. Commun. **147**, 190 (2002).

[7] G. Bartels, T. Unger, D. Kadau, D. E. Wolf, and J. Kertesz, Granular Matter **7**, 139 (2005).

[8] D. Wolf, T. Unger, D. Kadau, and L. Brendel, in *Powders and Grains*, edited by R. Garcia-Rojo, H. Hermann, and S. McNamara (A.A. Balkema, Leiden, The Netherlands, 2005), Vol. 1, pp. 525–535.

[9] F. A. Gilabert, J.-N. Roux, and A. Castellanos, Phys Rev E **75**, 011303 (2007).

[10] C. M. Kong and J. J. Lannutti, J. Am. Ceram. Soc. **83**, 2183 (2000).

[11] C. Martin and D. Bouvard, Acta Mater. **51**, 373 (2003).

[12] C. L. Martin, Acta Mater. **51**, 4589 (2003).

[13] C. L. Martin, D. Bouvard, and S. Shima, J. Mech. Phys. Solids **51**, 667 (2003).

[14] Z. Fournier, D. Gerimichalos, S. Herminghaus, M. M. Kohonen, F. Mugele, M. Scheel, M. Schulz, B. Schulz, C. Schier, R. Seemann *et al.*, Appl. Phys.: Condensed Matter **17**, S477 (2005).

[15] V. Richefeu, MoulaySaidEl. Youssoufi, and F. Radjai, Phys. Rev. E **73**, 051304 (2006).

[16] V. Richefeu, F. Radjai, and M. S. E. Youssoufi, Eur. Phys. J. E **21**, 359 (2007).

[17] S. Luding, Nature **435**, 159 (2005).

[18] R. Brewster, G. S. Grest, J. W. Landry, and A. J. Levine, Phys. Rev. E **72**, 061301 (2005).

[19] P. G. Rognon, J. N. Roux, D. Wolf, M. Naaim, and F. Chevoir, Europhys. Lett. **74**, 644 (2006).

[20] L. Aarons, Powder Technol. **183**, 340 (2008).

[21] P. G. Rognon, J. N. Roux, M. Naaim, and F. Chevoir, J. Fluid Mech. **596**, 21 (2008).

[22] M. Rock, M. Morgeneyer, J. Schwedes, D. Kadau, L. Brendel, and D. E. Wolf, Granular Matter **10**, 285 (2008).

[23] J.-L. Chermant, P. Odier, D. Jeulin, J.-P. Jernot, P. Lalanne, H. V. Damme, G. Nouet, and J.-Y. Laval, *Caractérisation des poudres et des céramiques* (HERMES, Paris, 1992).

[24] A. Donev, F. H. Stillinger, P. M. Chaikin, and S. Torquato, Phys Rev Lett. **92**, 255506 (2004).

[25] A. Donev, I. Cisse, D. Sachs, E. Variano, F. Stillinger, R. Connelly, S. Torquato, and P. Chaikin, Science **303**, 990 (2004).

[26] A. Donev, R. Connelly, F. H. Stillinger, and S. Torquato, Phys. Rev. E **75**, 051304 (2007).

[27] E. Azema and F. Radjai, Phys. Rev. E **81**, 051304 (2010).

[28] B. Saint-Cyr, J.-Y. Delenne, C. Voivret, F. Radjai, and P. Sornay, Phys. Rev. E **84**, 041302 (2011).

[29] CEGEO, B. Saint-Cyr, K. Szarf, C. Voivret, E. Azéma, V. Richefeu, J.-Y. Delenne, G. Combe, C. Nouguier-Lehon, P. Villard *et al.*, Eur. Phys. Lett. **98**, 44008 (2012).

[30] K. Shinohara, M. Oida, and B. Golman, Powder Technol. **107**, 131 (2000).

[31] A. A. Mirghasemi, L. Rothenburg, and E. L. Matyas, Geotechnique **52**, 209 (2002).

[32] K. Mair, K. M. Frye, and C. Marone, J. Geophys. Res. **107**, ECV 4-1 (2002).

[33] A. A. Pena, R. Garcia-Rojo, and H. J. Herrmann, Granul. Matter **9**, 279 (2007).

[34] C. Nouguier-Lehon, B. Cambou, and E. Vincens, Int. J. Numer. Anal. Methods Geomechan. **27**, 1207 (2003).

[35] P. Guo and X. Su, Can. Geotech. J. **44**, 579 (2007).

[36] E. Azéma, F. Radjai, R. Peyroux, and G. Saussine, Phys. Rev. E **76**, 011301 (2007).

[37] E. Azema, F. Radjai, and G. Saussine, Mech. Mater. **41**, 729 (2009).

[38] N. Estrada, E. Azéma, F. Radjai, and A. Taboada, Phys. Rev. E **84**, 011306 (2011).

[39] T. Pöschel, J. Phys. II **3**, 27 (1993).

[40] J. Favier, M. Abbaspour-Fard, M. Kremmer, and A. Raji, Eng. Computat. **16**, 467 (1999).

[41] R. P. Jensen, P. Bosscher, M. Plesha, and T. Edil, Int. J. Numer. Anal. Meth. Geomech. **23**, 531 (1999).

[42] I. Kock and K. Huhn, Sediment. Geol. **196**, 217 (2007).

[43] T. Sakakibara, S. Shibuya, and S. Kato, Powders Grains 2009 **1145**, 381 (2009).

[44] K. Maeda, H. Sakai, A. Kondo, T. Yamaguchi, M. Fukuma, and E. Nukudani, Granul. Matter (2010).

[45] F. Ludewig and N. Vandewalle, Phys. Rev. E **85**, 051307 (2012).

[46] L. Rothenburg, R. Bathurst, and A. Berlin, in *Powder and Grains*, edited by Thornton (Balkema, Rotterdam, 1993), pp. 147–153.

[47] J. Mitchell and K. Soga, *Fundamentals of Soil Behavior* (Wiley, New-York, 2005).

[48] S. Blott and K. Pye, Sedimentology **55**, 31 (2008).

[49] J. J. Moreau, Eur. J. Mech. A Solids **13**, 93 (1994).

[50] M. Jean, Comput. Methods Appl. Mech. Eng. **177**, 235 (1999).

[51] M. Kohonen, D. Geromichalos, M. Scheel, C. Schier, and S. Herminghaus, Physica A **339**, 7 (2004).

[52] F. Radjai and V. Richefeu, Philos. Trans. R. Soc. A **367**, 5123 (2009).

[53] B. Brogliato, *Nonsmooth Mechanics* (Springer, London, 1999).

[54] F. Radjaï, in *Physics of Dry Granular Media*, edited by H. J. Herrmann *et al.* (Kluwer Academic, Netherlands, 1998), pp. 305–312.

[55] F. Dubois and M. Jean, in *Actes du sixième colloque national en calcul des structures, CSMA-AFM-LMS* (Ecole Polytechnique, Giens, 2003), Vol. 1, pp. 111–118.

[56] F. Radjaï and E. Azéma, Eur. J. Env. Civil Eng. **13**, 204 (2009).

[57] I. Bratberg, F. Radjai, and A. Hansen, Phys. Rev. E **66**, 031303 (2002).

[58] A. Taboada, K. J. Chang, F. Radjai, and F. Bouchette, J. Geophys. Res. **110**, 1 (2005).

[59] C. Voivret, F. Radjaï, J.-Y. Delenne, and M. S. El Youssoufi, Phys. Rev. E **76**, 021301 (2007).

[60] C. Voivret, Ph.D. thesis, Université de Montpellier 2, 2008.

[61] E. Clement, Colloid Interface Sci. **4**, 294 (1999), current opinion.

[62] A. Castellanos, Adv. Phys. **54**, 263 (2005).

[63] J. Roux and F. Chevoir, *Discrete-element Modeling of Granular Materials* (Wiley-ISTE, New York, 2011), pp. 199–228.

[64] GDR-MiDi, Eur. Phys. J. E **14**, 341 (2004).

[65] J. C. Quezada, P. Breul, G. Saussine, and F. Radjai, Phys. Rev. E **86**, 031308 (2012).

[66] P. Hicher, H. Wahyudi, and D. Tessier, Comput. Geotech. **16**, 205 (1994).

[67] M. Oda and H. Kazama, Geotechnique **48**, 465 (1998).

[68] F. Calvetti, G. Combe, and J. Lancier, Mech. Cohesive. Frictional Mater. **2**, 121 (1997).

[69] J. Lanier and M. Jean, Powder Technol. **109**, 206 (2000).

[70] L. Rothenburg and R. J. Bathurst, Geotechnique **39**, 601 (1989).

[71] R. J. Bathurst and L. Rothenburg, Mech. Mater. **9**, 65 (1990).

[72] F. Radjai, I. Preechawuttipong, and R. Peyroux, in *Continuous and Discontinuous Modeling of Cohesive-Frictional Materials*, edited by P. Vermeer, S. Diebels, W. Ehlers, H. Herrmann, S. Luding, and E. Ramm (Springer, Berlin, 2000), pp. 149–162.

[73] F. Radjai, H. Troadec, and S. Roux, in *Granular Materials: Fundamentals and Applications*, edited by S. Antony, W. Hoyle, and Y. Ding (The Royal Society of Chemistry, Cambridge, 2004), pp. 157–184.

[74] F. Radjai, D. E. Wolf, M. Jean, and J.-J. Moreau, Phys. Rev. Lett. **80**, 61 (1998).

[75] Q. Li, V. Rudolph, B. Weigl, and A. Earl, Int. J. Pharmaceut. **280**, 77 (2004).

[76] J. Moreau, in *Novel Approaches in Civil Engineering*, edited by M. Frémond and F. Maceri (Springer-Verlag, Berlin, 2004), pp. 1–46.